POLITECNICO DI TORINO

Master's Degree in Energy Engineering

Politecnico di Torino

Mondragon Unibertsitatea

Master's Degree Thesis

Advanced offshore renewable energy resource assessment, combining re-analysis datasets with bias correction techniques, analysing the sensitivity of these techniques to the provided data

Supervisors

Prof. Giuseppe GIORGI

Prof. Markel PEÑALBA

Candidate

Francesco CALLEA

JULY 2024

Abstract

The present work focuses on the necessity of a deep and accurate knowledge of metocean conditions for Offshore Renewable Energy devices. *In-situ* measurements are accurate, but often not-available or expensive to obtain on a large time-scale, *reanalysis datasets* are characterized by an intrinsic uncertainty. Combining both via downscaling techniques where the direction of waves has a significant effect seems to be the most sensible choice to obtain reliable and long-term metocean datasets. Therefore, the possibility to consider wave direction in bias correction methods was analyzed. The results of three directional strategies were implemented; their results (centred on the *significant wave height*'s correction) were computed and compared across four locations around the Iberian peninsula (each offering different wave and wind characteristics for an optimal cross-validation) according to apposite statistical parameters. A comparison was made with the most performing non-directional technique and improvements in the data quality were actually observed in most methods, with the Gumbel-based techniques generally outperforming the linearly-spaced ones.

The study also addressed the selection of the most appropriate time window for the calibration: more specifically, the *duration* (*i.e.* number of years) and the *instant* (*i.e.* exact time period) of the selected time window for the identification of correction factor. The identification of correction factors from a given window, and their application in successive windows was addressed as well.

A temporal sensitivity analysis was therefore carried out, considering two different application periods (2015-2019 and 2019-2023) to cross-validate the results obtained in each case. Results showed that the length of the required window may be shorter than expected, although the instant is to be carefully selected: corrections based on only 1 year of historical observations already provide satisfactory results, although the dispersion among the different selected periods is still large. This dispersion significantly reduces as more years of data are used, regardless from the selected period, to the point when further enlarging the identification window brings little to no significant improvement to the bias correction.

One more verification was carried out, assessing whether the identification window could be shortened down below one year (*i.e.* half a year or a single season), in order to make the observation process cheaper without reducing efficiency. Hence, each season was analysed and compared against each other. That way, it was observed that, overall, correction factors based on the winter months better encompass the variety of wave heights (and relative distribution) and provide satisfactory correction factors for metocean data calibration close to the results obtained by identifying correction factors based on a full-year dataset.

Table of Contents

List of Figures

Chapter 1

Introduction

A strong and decisive transition from a fossile-based towards a cleaner and more sustainable energy production strongly relies on the development of Renewable Energy Sources (*RES*). Fossil fuels, in fact, still account for a vast majority of global electricity production.
Several mature and performing technologies, such as solar and wind energy, already exist and provide an important contribution in the diversification of the energy supply. According to the International Renewable Energy Agency (IRENA), in order for this transition to be carried out properly, the total global installed capacity of renewable energy needs to increase by a factor of five, equivalent to 14 TW by 2050 [1].
Furthermore, a relevant addition is expected to come from technologies that are yet to be fully exploited: the International Agency estimates that about 45% of CO_2 emission savings by 2050 will come by technologies currently under development [2].

Offshore Renewable Energies (*OREs*) appear a valid option to support this transition in a viable way. Onshore wind energy, in fact, has already affirmed itself as a safe, consistent and reliable energy source. As a response to increasing land-exploitation issues, though, and to take advantage of the higher and more stable wind regimes in the open sea, an expansion towards offshore installations is currently undergoing and developing at a very high rate. It is, in fact, expected to multiply its current worldwide installed capacity by 30, over the next 30 years [1].
Aside to offshore wind turbines (both *bottom-fixed* and *floating*), wave energy and tidal energy are projected to significantly increase their percentage in the future energy mix, eventually covering up to 10% of the global electricity demand [3].
Both wave energy converters (WECs) and tidal energy devices, even including floating offshore wind turbines (*FOWTs*), still require strong improvements to actually become competitive on the market. These include:

- Optimization of the design of floating structures, possibly reducing materials use, while preserving their reliability and structural integrity;
- Increasing the energy generation capacity through the use of nonlinear hydrodynamic models in the design of control algorithms;
- Enhancing the durability of design key components, such as mooring lines and power take-off (PTO) systems via the utilization of new materials, and designing them to operate within more efficiently-adjusted regions;
- Improving accessibility and availability through the optimization of operation and maintenance ($O\&M$) strategies.

Hence, it becomes clear that, to effectively target and solve any structural stability and accessibility issue, an accurate evaluation and knowledge of the climate (and, in particular, wave) conditions in the area becomes extremely important.

The focus is therefore put over the resource assessment stage of a energy plant's design process, and its strong need for accurate *metocean data*. Being the first step into the conversion chain of every ORE system, the error introduced by metocean data in this stage propagates to the development of the whole chain itself. Since this stage already features a very high uncertainty level, the risk is to become excessively conservative, resulting in technologies being too large and expensive and, because of this, not competitive on the market [4].
Offshore renewable technologies are typically designed for two operational modes: power production mode (PP) and survivability mode ($Surv$). The former refers to the condition where power production is safely enabled, while the latter addresses the conditions where the risk of damaging the ORE system is high and protecting the device becomes a priority. Acknowledging this, reducing the uncertainty related to metocean across the whole operational domain, including both regions, is of high-relevance.
As climate conditions are also affected by spatio-temporal variations (including inter-annual and intra-annual variability), and being them a potentially non-stationary resource, long datasets are required for a better understanding of the resource in a given region. The International Organization for Standardization (ISO) suggests a minimum of 10 years of data (equal to 25% of the return period of interest) for ORE systems with a lifespan of 20-30 years [5], while the Institute of Marine Engineering, Science & Technology (IMAREST) recommends an even longer period, equal to 30 years, to accurately characterize most extreme events [6].

The data gathering process typically relies on two sources:

- One hand, *observation buoys* allow the recording of sea-states with a very high level of accuracy. They display some disadvantages though: first, such long

periods as the ones requested for ORE systems' lifespan are typically complex and very expensive to obtain. Furthermore, due to the harsh environment in the open ocean, the equipment working within observation buoys might fail, resulting in eventually large periods of unavailable data;

- on the other hand, *re-analysis datasets* and data from climate models (also referred to as *simulated datasets*) can also be used. They offer extremely good temporal (some go back to 1900 [7] [8]) and spatial (virtually every point in the world can be covered) coverage for no cost. Their main issue is related to the limited accuracy, especially during extreme weather conditions or in particular micro-climate areas.

This issue makes it necessary to establish some calibration techniques, based on observation datasets, whose aim is to reduce the difference (*bias*) between buoy data and simulation data.

To our knowledge, a comprehensive review of such calibration techniques applied to ocean waves is presented by Lemos et al. [9], with reference to the ERA5 re-analysis dataset developed by Copernicus. A successive study, carried out by Penalba et al. [10] presented an extension of that study, with a focus on the ORE sectors and using *in-situ* measurements at four different locations for the assessment of the different BC techniques. It also introduced specific statistical metrics (for instance, *PDFscore* and the *Distribution Added Value*) for BC techniques' evaluation.
The present study comes with multiple goals in the field of bias correction of metocean data:

1. Further explore and develop the possibility of using bias correction techniques, eventually accounting for wave direction, as already introduced by Lemos in his work [9];

2. Asses the effectiveness of aforementioned techniques, carrying out a performance comparison across four different locations around the Iberian peninsula;

3. Carry out a sensitivity analysis evaluating how the bias correction can be affected by the duration and the instant of the chosen reference data.

Chapter 2

Bias Correction Techniques

Previous works from both Lemos et. al [9] and Penalba et al. [10] already performed a first attempt of applying statistical tools to raw metocean data, with the aim of adjusting them to match the statistical properties of the reference dataset. While Lemos' work uses the Global Ocean Waves 2 (GOW2) wave hindcast [11] as a historical reference, measurements from observation buoys are here assumed as *ground truth* (from here on referred to as y^{obs}), in accordance with Penalba's study [10].
These techniques, which are merely statistical methods, have started receiving increasing attention over the last 20 years [12], given their relatively simple application and the fact that they do not require a deep understanding of the physics model nor of the data assimilation methods [13].

2.1 Basic BC techniques' overview

Penalba's and Lemos' papers firstly carried out a detailed assessment and comparison of some bias correction techniques; four methods have been addressed by both, their results have been computed and compared, to verify which would perform better. Following, their principles are shortly introduced and explained:

a) The *Delta-change* technique, first suggested in [14], is the simplest BC technique. It consists of adjusting the *assimilated dataset* (here representing the ERA5 one) y^{as} by adding a constant correction factor (the *Delta-factor*) to every point of the dataset.
Specifically, the Delta-factor is computed as the subtraction between the average values of the assimilated ($\hat{y}^{\text{as}}$) and the observation dataset ($\hat{y}^{\text{obs}}$).
Hence, the corrected dataset will be given by the following equation:

$$y_i^{BC} = y_i^{as} + (\hat{y}^{obs} - \hat{y}^{as}), \tag{2.1}$$

where i=1,...,N, N being the number of points considered from the dataset. In this study, y represents H_s, but it can be referred any other metocean quantity (for instance, wind speed U_w, peak period T_p and so on).
This method, although being the simplest and easiest to be applied, turned out to be the least effective as well [9] [10]. In fact, the correction factor being constant whatever the wave height, means the Delta-factor might be effective for some low to intermediate wave heights, but it will be almost completely ineffective if used to correct harsher weather conditions.

b) The *Full Distribution Mapping* (*FDM*) is the simplest method within the ones belonging to the distribution mapping group. In these, the correction factor is computed as a function of the correlation between the assimilated cumulative density function (CDF_{as}) and the observed CDFs (CDF_{obs}). In the full distribution mapping, the whole CDF is considered to identify the statistical correlation X^{FDM}, which is computed as the difference between the inverse CDF of the assimilated and the observed datasets:

$$X^{FDM} = CDF_{as}^{-1} - CDF_{obs}^{-1}. \tag{2.2}$$

An n-order polynomial function is used to fit the statistical relationship, to transform X^{FDM} into time-domain correction factors to be applied point-by-point to the assimilated dataset. Therefore, the corrected output is:

$$y_i^{BC} = y_i^{as} + f(X^{FDM}, n), \tag{2.3}$$

where f is the polynomial function, and n is the order of the function itself. Just as the previous, FDM is not able to fully cover the whole dataset's needs, due to a predominance of milder wave conditions in the distribution.

c) The *linearly-spaced quantile mapping* (*QM*) is based on the same principles as the FDM; the difference is that here the CDF is divided into *quantiles*, with the correction factor $X^{QM}(q_i)$ being identified at each of them, as shown in Figure 2.1.
Correction factor is therefore computed at each quantile, and later incorporated in the time-domain, similarly to what done in the FDM, as in the following equations:

$$X^{QM}(q_i) = CDF_{as}^{-1}(q_i) - CDF_{obs}^{-1}(q_i) \tag{2.4}$$

$$y^{BC}(q_i) = y^{as}(q_i) + f(X^{FDM}(q_i, n) \tag{2.5}$$

d) The *Gumbel quantile mapping* (*GQM*), finally, maintains the same concept of the QM technique just shown, adopting a different quantile distribution. The Gumbel quantile distribution [15] is defined as:

$$F(x, \mu, \beta) = e^{-e^{-(x-\mu)/\beta}}, \tag{2.6}$$

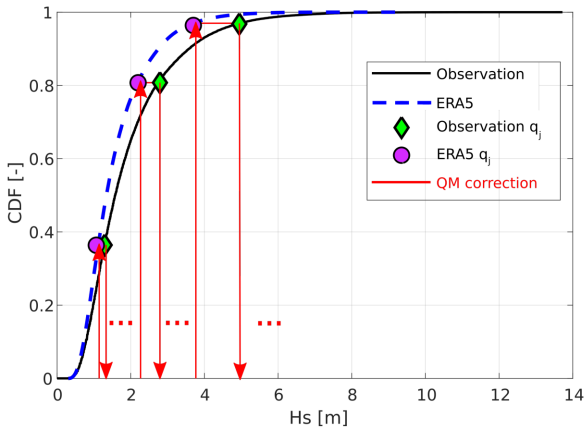

Figure 2.1: Schematic representation of the quantile mapping technique.

where μ and β are the location and scale parameters, respectively. The Gumbel distribution places over 50% of the quantiles above the 99^{th} quantile, ensuring a better representation of the upper tail of the distribution (=highest wave heights), as shown in Figure 2.2. Once quantiles are defined, the remaining part of the BC technique is carried out as previously illustrated for the quantile mapping method. The large number of quantiles above the 90^{th} ensures a significantly better correction of the highest wave heights, where most important biases are usually found.

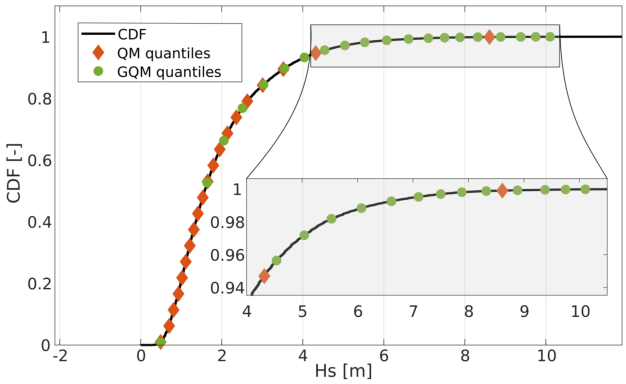

Figure 2.2: Comparison between linear and Gumbel quantile distribution.

The first (and simplest) of these techniques, that do not perform any subdivision when calculating the correction factors, were proven not to be adequate (as [9] [10] show). Quantile Mapping, whether making use of the linear or the Gumbel distribution for quantile identification, was found to suit much better the bias

correction necessities for metocean data, as the identification of a correction factor per each area of the distribution allowed for a higher improvement of the data's quality.
Nevertheless, as Lemos' paper [9] pointed out first, there might be the necessity for a BC technique that uses wave direction as a distinction criterion as well, as each sector of the wave rose can possibly display a different H_s distribution, hence, require a separate correction factor calculation process.

In the following section, this required is dealt with, presenting three techniques that first perform a distinction of the wave rose into *sectors*, to then carry out the correction process.

2.2 Directionally Adjusted Quantile Mapping

The techniques seen until this point only use univariate H_s metocean data. The work from Minguez et al. [16] pointed out that climate simulations can perform differently for waves coming from different directions; close to coastal regions, in particular, where wind speed might not be strong enough to generate local wind-waves, and where swell components coming from waves generated in further regions can get too, the resolution is likely to be lower.
More studies suggested that a directional calibration of wave data can be useful in the open ocean as well, where swell components (possibly coming from multiple directions) are predominant [17] [18], and where long-term evolution of the swell itself may be treated poorly by simulation [19].
Minguez et al. first proposed a solution [16], later brought up again by Lemos, for accounting directionality in bias correction techniques. The present work bases itself on the innovations introduced in the aforementioned papers.

A very important difference between the previous techniques and the ones addressed here is the use of the *nonlinear regression* as a mathematical method for correction factors identification. While, previously, the correlation between the two CDFs was a polynomial function, nonlinear regression finds the factors varying smoothly across the range of wave directions by the means of a cubic spline:

$$y^{BC} = a^{DAQM}(\theta)(y^{sim})^{b^{DAQM}(\theta)} \tag{2.7}$$

where a^{DAQM} and b^{DAQM} are the spline parameters that vary depending on the wave direction θ under analysis. An objective function, in this case the sum of square residuals, is targeted; the solution of the optimization problem returns the

calibrated values of the variable y as follows:

$$min(a,b) = [\sum (y_i^{obs} - y_i^{sim})^2] = \sum [y_i^{obs} - a_i^{DAQM}(\theta_i)(y_i^{sim})^{b_i^{DAQM}(\theta_i)}]^2, i = 1, ..., S \tag{2.8}$$

where S is the number of sectors the wave rose is divided in.

All techniques imply wave data to be rearranged in various sectors, depending on the wave direction; after this, each sector is divided into quantiles, similarly to the QM and GQM methods, so that the correction is never calibrated on the whole dataset available. Also, a couple of average correction factors $a(\theta, q_i)$ and $b(\theta, q_i)$ is always computed, as each quantile subdivision may display a different number of re-analysis and observation data. All of the following techniques have been evaluated using both a linear and a Gumbel quantile distribution, similarly to what done in the non-directional analysis.

- the first, and simplest, of directional techniques evaluated here has been referred to as "*Directionally Adjusted Quantile Mapping 1*" (*DAQM1*). It involves the creation of, in this case, 60 directional *non-overlapping* sectors, as simply shown in Figure 2.3.

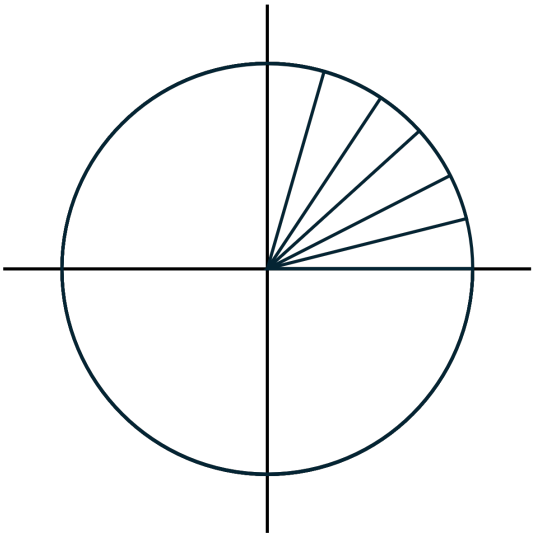

Figure 2.3: Sectors subdivision in the DAQM1 technique.

Per each sector, 50 quantiles are identified on the basis of the observed data distribution, whose wave height values are rearranged accordingly. The indices corresponding to each H_s are stored and used to perform the same subdivision for the simulated dataset as well. Since the two display a different data

distribution, this is necessary to ensure that each SWH is corrected with the correspondent value in the other dataset.
After this, the nonlinear regression problem is solved; average correction factors are stored per each quantile and used to calibrated re-analysis wave values.
The technique has been assessed both with a linear quantile distribution (in this case, simply referred to as *DAQM1*) and with a Gumbel one (the acronym *DAGQM1* is used here).

- The second technique is here referred to as "*Directionally Adjusted Quantile Mapping 2*" (*DAQM2*; *DAGQM2* in his Gumbel distribution variant). It was the only one already developed in a previous analysis [9]; its effectiveness has here been re-assessed, with different datasets than the first case (Lemos, in fact, adopted a global hindcast as ground truth; in-situ measurements are used here). The method divides the wave rose into 360 rotating sectors, rotating around the directional circumference 1° at a time, each of them 22.5° wide (Figure 2.4 provides a visual representation of this data rearrangement).

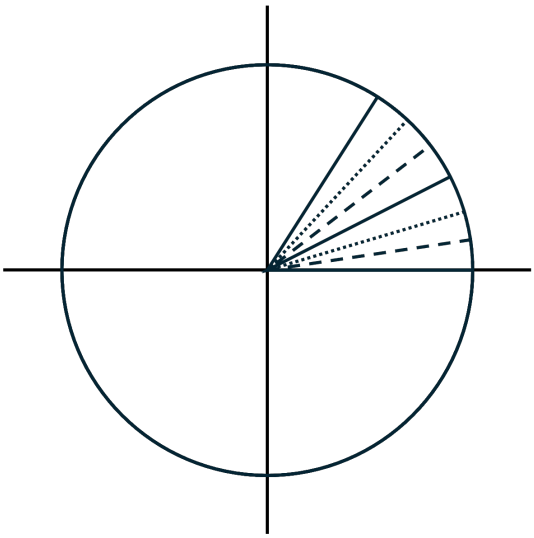

Figure 2.4: Sectors subdivision in DAQM2 technique.

As in the DAQM1 technique, a quantile subdivision followed by the resolution of the nonlinear regression problem is carried out for each sector. Here, having multiple wider sectors rotating 1° at a time (hence, *overlapping*), results in each wave height data being included in multiple sectors, and therefore separately undergoing various corrections. In the absence of a strict criterion, in this work each of the outcoming calibrations has been compared with the buoy data: the one displaying the lowest absolute bias has been selected and stored in the output array, providing the calibrated metocean dataset.

- The last of the three techniques has been called "*Directionally Adjusted Quantile Mapping 3*" (*DAQM3*; *DAGQM3*, for his Gumbel distribution equivalent). Picking up some elements from both previous options, the directional circumference is divided into 360 sectors, non-overlapping, each 1° wide. In this case, they will be referred to as *application sectors*, as for each of them, a wider (22.5°) *identification sector*, sharing its same center, is defined, as shown in Figure 2.5.

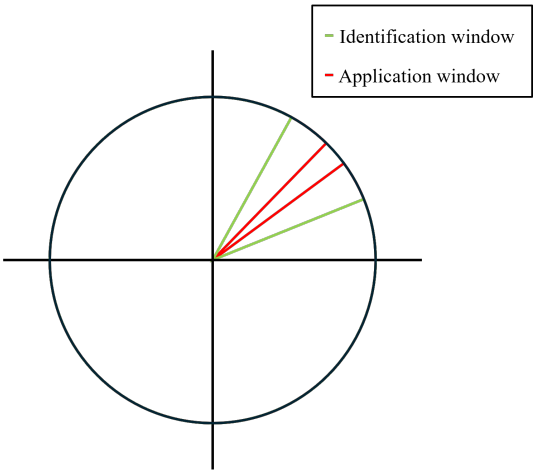

Figure 2.5: Sectors subdivision in DAQM3 technique.

  In the picture, the smaller red one is the application sector, while the bigger green lines represent the identification sector. The latter gathers all data in a bigger portion of the wave rose than the one that will actually be corrected, and uses them (in an analogue way as the previous techniques) to compute and identify the correction factors, with the aim of eventually having a higher quantity of information in those regions where only few samples are available. Identification sectors ending up overlapping does not represent an issue, in this case, as data are only corrected within the application ones, hence, each H_s value will only be calibrated once.

In this work, calibration via each of the three presented techniques (with their Gumbel counterparts) has been done. Aside to them, non-directional quantile mapping has been applied too as a reference that does not consider wave direction. The following chapter shows the case-study, metrics and results of the bias correction procedures.

Chapter 3

Benchmarking of Bias Correction techniques

In this section, the basis for BC techniques assessment are set. The case study is presented, shedding light on the location choice and data selection process; then, statistical and graphical tools for techniques' performance evaluation are illustrated and explained. Finally, bias correction results are shown and commented.

3.1 Verification case study

The reason why directionality was incorporated in the bias correction techniques' structure is to provide an additional contribution in the cases where the wave rose does not display a predominant incoming wave direction, rather a smoother shape, where data associated to different spatial orientations show distinct distributions: those are the cases where each sector is likely to need a dedicated calibration, independent from the others and from the dataset as a whole.

For the present study, four locations around the Iberian peninsula have been considered, as shown in Figure 3.1. Re-analysis data are obtained from the ERA-5 model produced by the European Centre for Medium-Range Weather Forecast, while observation data are provided by the Spanish Port Authority coordination agency "Puerto del Estado".
Even though the temporal resolution is identical, since measurement buoys are subjected to failure and can provide uncovered time periods with unavailable data, a pre-processing has been necessary. Missing values have been treated differently, depending on their quantity. When one single point was missing, its value has been interpolated to fill then gap; in the case of a wider time range with no data recorded, the period has been omitted, and neglected during the calibration process.

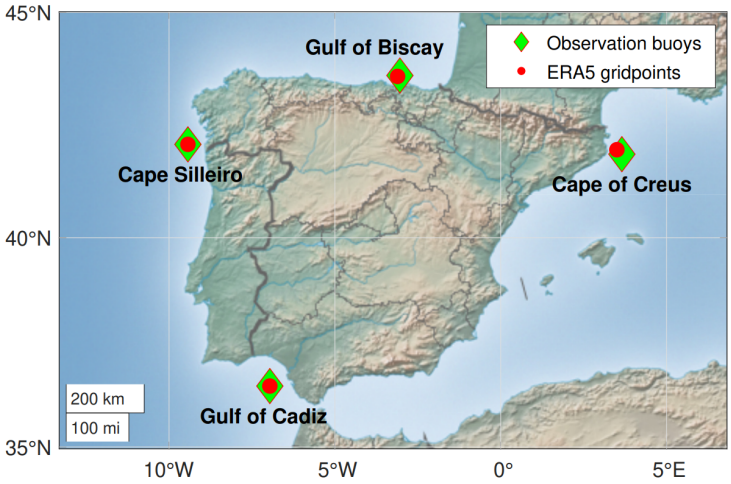

Figure 3.1: Case study location; large green diamonds represent measurement buoys, while small red dots correspond to the ERA-5 re-analysis gridpoints [10].

Past studies mainly focused on the data processing in the Gulf of Biscay site: even though it represents a relatively sheltered area in north-eastern Atlantic Ocean, mostly influenced by swell waves ($\hat{H}_s = 1.9m$ and $\hat{T}_p = 9.6s$) [10], it has already been considered of high interest for the installation of several ORE technologies, as demonstrated by the Mutriku Wave Power Plant [20] and by the pre-commercial FOWT farm promoted by Saitec Offshore Technologies [21].
Aside from Gulf of Biscay (already introduced, mainly dominated by swell waves and consistent wind speeds), the others are:

- *Cape Silleiro* to the west, facing the coast of Galicia, an open area dominated by even larger swell waves ($\hat{H}_s = 2.4m$ and $\hat{T}_p = 9.8s$) and consistent wind speed ($\hat{U}_w = 6m/s$);

- *Gulf of Cadiz* to the south, in a more enclosed area next to the Strait of Gibraltar, is governed by a combination of swell waves and wind seas, the second slightly predominant (($\hat{H}_s = 1.2m$, $\hat{T}_p^{swell} = 10s$ and $\hat{T}_p^{wind} = 5s$ approximately). Wind resource here is consistent too, just as in previous cases ($\hat{U}_w = 5.3m/s$);

- *Cape Creus* to the east, in the Mediterranean coast facing Catalonia, much more dominated by wind seas ($\hat{H}_s = 1.3m$ and $\hat{T}_p = 5.5s$) and less consistent wind speed, showing higher variability (distribution tails going up to $20m/s$) resulting in a higher mean wind speed ($\hat{U}_w = 6.1m/s$).

The adoption of several locations for validating is necessary, as it is crucial to make sure not to run into the case where directional techniques work very well with a specific wave distribution, but do not suit others with a different distribution. Therefore, trying them out in conditions with very different wave roses is useful, as it provides a very good cross-validation and, eventually, indications about whether directional calibration methods work better with a specific wave occurrence distribution. Following, Figure 3.2 reports the occurrence scatter diagrams of the observed H_s-T_p combinations for each of the analysed locations:

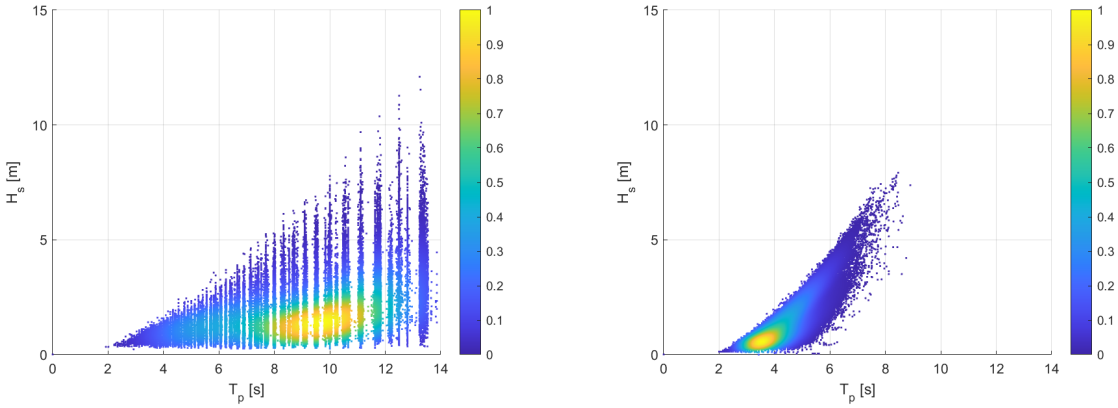

(a) Gulf of Biscay.

(b) Cape Creus.

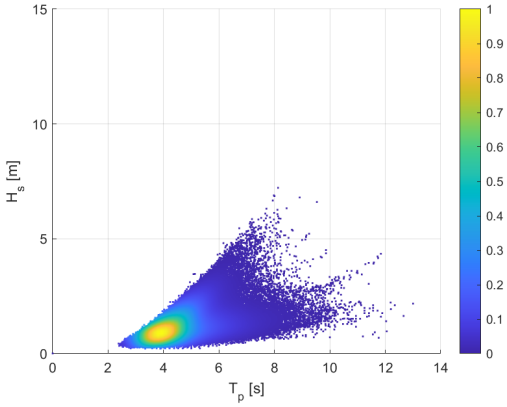

(c) Gulf of Cadiz.

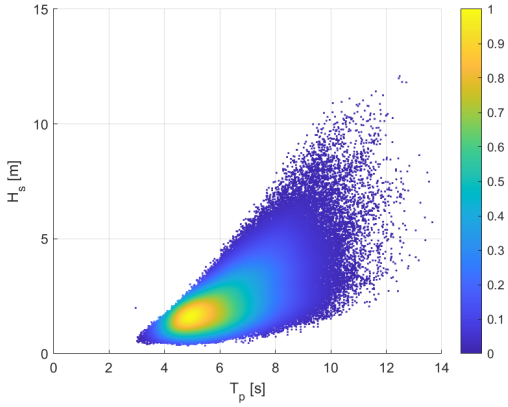

(d) Cape Silleiro.

Figure 3.2: H_s-T_p scatter diagrams of the four locations analysed around the Iberian peninsula.

Most common wave height values appear quite low for all locations, with few differences from this point of view; the prevalence of wind seas on Cape Creus and Gulf of Cadiz (Fig. 3.2b and 3.2c, respectively) data, though, appears very clearly

when the lower peak periods are looked at; Cape Creus' most common T_p values are between 3 and 4 s, while Gulf of Cadiz shows an average of around 4 s. Swell waves, on the other hand, are predominant in the Cape Silleiro and Gulf of Biscay areas, where much longer waves are present (around 5 s for Cape Silleiro and even between 8 and 10 s in Gulf of Biscay) and display a broader distribution, with higher peaks in terms of significant wave heights as well.
The influence of wave direction on the application of bias correction techniques (and its assessment over various case studies) can be of vital importance as well, if accounting for the different distribution that characterize each sea area. Hence, Figure 3.3 represents the wave roses (produced basing on observation datasets) for the four locations analysed (already shown in Figure 3.1):

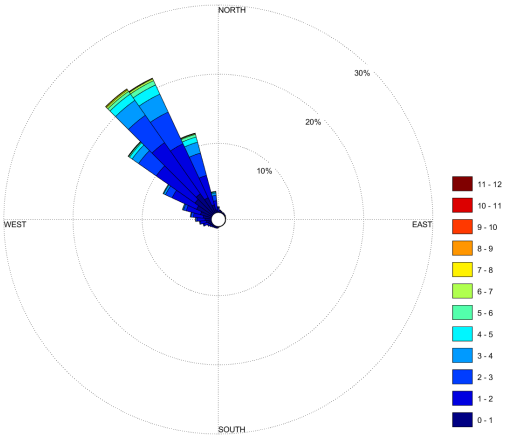

(a) Wave rose for Gulf of Biscay.

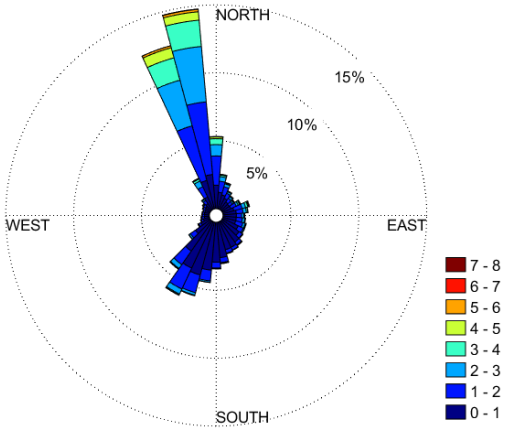

(b) Wave rose for Cape Creus.

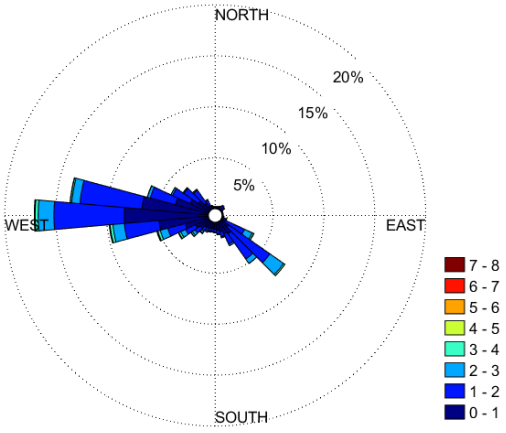

(c) Wave rose for Gulf of Cadiz.

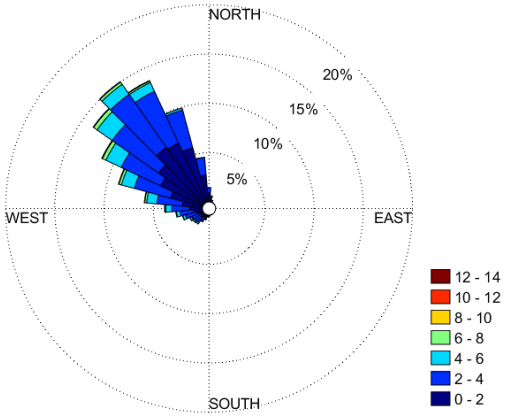

(d) Wave rose for Cape Silleiro.

Figure 3.3: Wave roses of the four locations analysed around the Iberian peninsula.

It is clear that, as Figures 3.3a and 3.3d show, Gulf of Biscay and Cape Silleiro display a predominance of waves coming from the North-West direction, being fully exposed to the Atlantic Ocean from that side. Things are different in the Gulf of Cadiz measurement buoy, as the presence of the landmass to its north represents a shield that prevents wave formation from that direction; hence, a fully western-driven wave provenience is there, with a smaller peak of waves coming from South-East (where a slightly more open area allows propagation from that side). Cape Creus, finally, is the only one in the Mediterranean Sea: due to the coast's presence to its left, it is the only one that doesn't show a strong wave presence in that direction. As winds at those intermediate latitudes rarely blow from east to west, northern waves are the most common here, with a slight component found in South-West as well.
Looking at the scale of each wave rose, it is also evident that much higher waves can be encountered in Cape Silleiro and Gulf of Biscay. This is likely due to their belonging to a more open portion of sea, with respect to the other two locations (that are, instead, situated in closer basins), where it is easier for swell waves to propagate and reach the target locations undisturbed and without significant energy losses.

3.2 Evaluation metrics

The first and most important indicator, on which the whole analysis here presented is based, is of course the bias, meant as the difference, per each point, between the value obtained from the reanalysis model and the one recorded *in-situ* by the measurement device (observation buoy, in this case). In order to allow a more complete and easy-to-understand comparison between each technique and, within them, each location, some more specific quantities have been considered and computed in each case study. They are here presented:

1. Most essential metric is the *mean bias*, simply obtained as the average, computed over the whole dataset, over the single-point difference between observation (ground-truth) and simulation data; later on, corrected values are looked at (instead of the latter simulated ones), to evaluate the improvements brought by the techniques' application:

$$bias_{mean}(y^{obs}, y^{sim}||y^{BC}) = mean(y^{sim}||y^{BC} - y^{obs}). \tag{3.1}$$

   In several plots, the mean bias computation has been performed at each quantile, in order to observe how different zones of the distribution would be affected differently by the bias correction procedure. In that case, the

operation performed would be as:

$$bias_{mean}(q_i)(y_{q_i}^{obs}, y_{q_i}^{sim}||y_{q_i}^{BC}) = mean|_{q_i}(y_{q_i}^{sim}||y_{q_i}^{BC} - y_{q_i}^{obs}). \tag{3.2}$$

2. Strictly related to the bias, the *dispersion* tells how "wide" the single-point bias distribution is. After having computed the bias for each value of the dataset, the dispersion is obtained as the difference between the 75^{th} and the 25^{th} quantile:

$$dispersion = q_{75}(bias(y_{q_i}^{obs}, y_{q_i}^{sim}||y_{q_i}^{BC})) - q_{25}(bias(y_{q_i}^{obs}, y_{q_i}^{sim}||y_{q_i}^{BC})). \tag{3.3}$$

   A higher dispersion suggests the presence of many different values of bias for different parts of the datasets; it may indicate that some sea-states are better represented (or corrected, if $y_{q_i}^{BC}$ is being considered) than others, and that appositely tailored correction techniques are necessary.

3. Despite the mean bias being simple and easy to calculate, the work by Penalba et al. [10] introduced two more specific and more statistic-oriented metrics. The first of them is the PDF_{score}, evaluating the similarity between two PDFs, which allows for a more complete comparison across the whole distribution [22]:

$$PDF_{score} = \sum_{m=1}^{M} min(PDF(y_m^{obs})) - PDF(y_m^{as}). \tag{3.4}$$

   where M is the number of bins used to represent the PDF.

4. The *DAV* (*Distribution Added Value*), instead, allows for a normalized comparison between the two PDF_{score}s as follows:

$$DAV = \frac{PDF_{score}^{BC} - PDF_{score}^{as}}{PDF_{score}^{as}} \times 100, \tag{3.5}$$

   where PDF_{score}^{BC} and PDF_{score}^{as} represent the PDF_{score}s for the corrected and raw assimilated datasets, respectively. The DAV is particularly useful here, as it provides a direct information about the improvement brought by the implementation of each bias correction technique

3.3 Benchmarking results

As previously explained, all the directional techniques previously introduced, plus linear quantile mapping, have been applied; each of them with both linear and Gumbel quantile distribution, for 8 total techniques employed (in each location). For a clear visualization of the results, the whole wave rose has been decomposed

in 360 sectors for the representation, each 1° wide. This has been applied to non-directional techniques as well, to allow a direct comparison among all correction methods. For each direction, the distribution has been divided in 50 linearly spaced quantiles; the average bias has been computed in each of them and represented on a 3D heatmap. In Figure 3.4, for a reference, the simulated data's bias for each of the four locations is represented. Data from years 2010-2019 have been used:

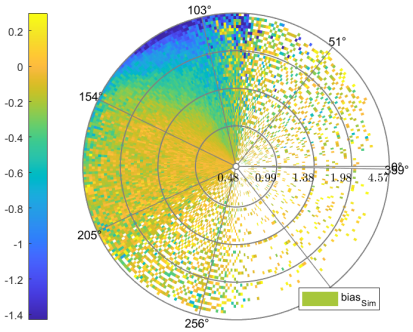

(a) Simulation bias for Gulf of Biscay.

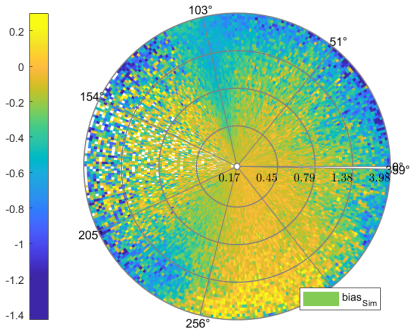

(b) Simulation bias for Cape Creus.

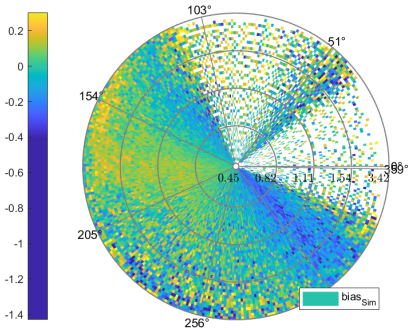

(c) Simulation bias for Gulf of Cadiz.

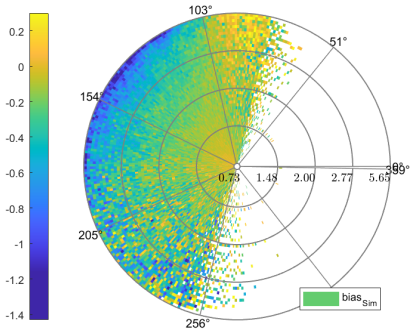

(d) Simulation bias for Cape Silleiro.

Figure 3.4: Simulation bias in the four locations analysed around the Iberian peninsula.

As shown, in most of the direction/quantile combination, reanalysis datasets model significant wave height values with an acceptable accuracy (bias lower than $0.2m$) in most regions of the plots. There is, though, a non-negligible tendency to underestimate wave height, in all locations, which gets even more relevant at higher quantiles (especially, as Figures 3.4a and 3.4d highlight) in Gulf of Biscay and Cape Silleiro, where the predominance of the swell component results in higher peak values; here,

bias reaches down to $-1.4m$ in some of the highest quantiles (which can be significant). The poor performances in the upper tails of the distribution calls for the necessity of appositely suited correction techniques, both in terms of wave direction (as the trend is accentuated in the regions with the highest frequency of incoming waves) and quantile definition (hence, the adoption of the Gumbel distribution too).

For the first part of the work, all correction methods have been tried on the Gulf of Biscay dataset, as it already was the basis of several previous analyses; after this, the conclusions obtained have been validated over the remaining locations. Figure 3.5 shows the quantile-quantile (Q-Q) plots, in the Gulf of Biscay analysis point, for each of the techniques adopted.

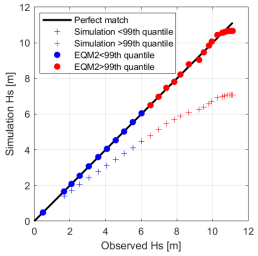

(a) EQM technique.

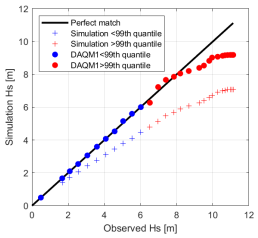

(b) DAQM1 technique.

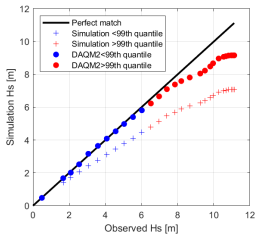

(c) DAQM2 technique.

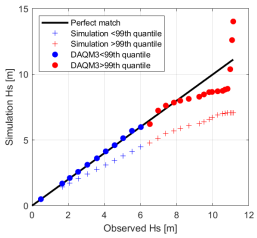

(d) DAQM3 technique.

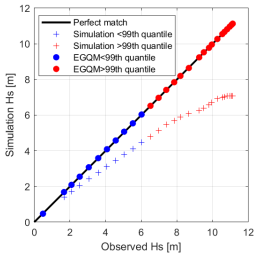

(e) EGQM technique.

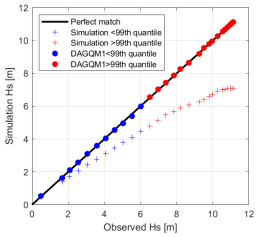

(f) DAGQM1 technique.

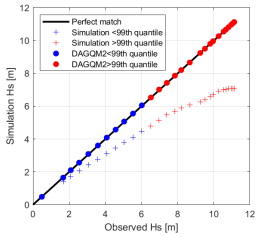

(g) DAGQM2 technique.

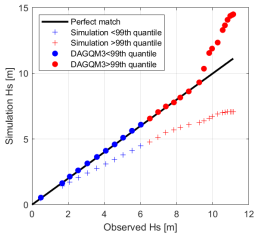

(h) DAGQM3 technique.

Figure 3.5: Q-Q plots for each bias correction technique (*linear* quantile distribution above, *Gumbel* quantile distribution below). Crosses represent to the raw assimilated dataset, while dots represent values after techniques' application. The blue and red circles refers to quantiles below and above the 99^{th}, respectively.

For what linear distribution techniques are concerned, all of them provide a significant improvement with respect to the raw reanalysis dataset. There is a good correspondence between simulated and observed data below the 99^{th} quantile, although they do not display the same correction ability when it comes to extreme events (with non-directional quantile mapping actually being the best of them).

All Gumbel distribution techniques (except for the one in Figure 3.5h), instead, tackle the higher-quantiles issue very well, managing to accurately capture higher wave heights without losing focus over the lower and intermediate quantiles (no significant differences between non-directional and directional methods are deduced from these graphs).

To better visualize how each technique performs along each direction of the wave rose, and to provide a better insight on whether accounting for directionality actually improves bias correction performance in wave data, Figures 3.6 and 3.7 show the same type of mean bias per each quantile and direction as in Figure 3.4; this time, each heatmap represents the result of a different bias correction technique over the same Gulf of Biscay dataset (with a linear quantile distribution, for Figure 3.6, and with a Gumbel one in Figure 3.7).

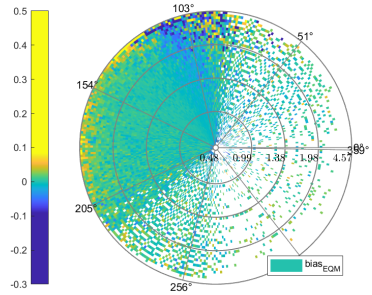

(a) Linear quantile mapping bias for Gulf of Biscay.

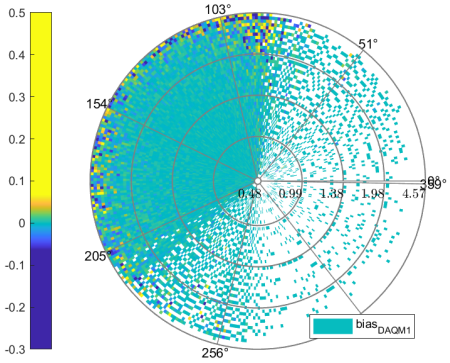

(b) DAQM1 bias for Gulf of Biscay.

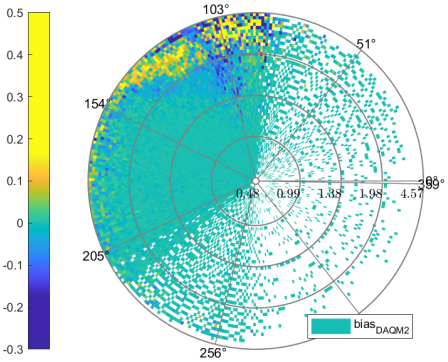

(c) DAQM2 bias for Gulf of Biscay.

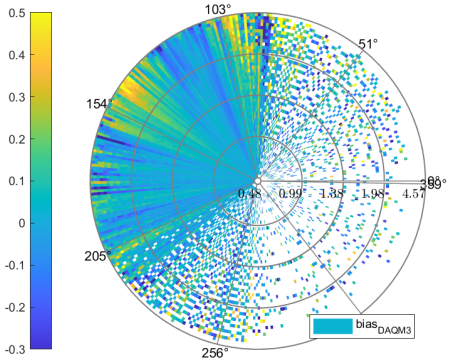

(d) DAQM3 bias for Gulf of Biscay.

Figure 3.6: Mean bias, per quantile and direction, for each bias correction technique (*linear quantile distribution*).

From these plots, it is already clear that, aside from Fig. 3.6d, all techniques bring a reduction in the bias of simulation dataset, reaching a value close to zero in most direction and wave heights. It is also clear, on the other hand, that upper quantiles still experience an uncertainty (either under or overestimation), that definitely makes the Gumbel-based techniques' application necessary.

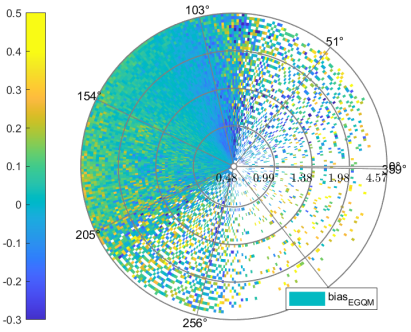

(a) Gumbel quantile mapping bias for Gulf of Biscay.

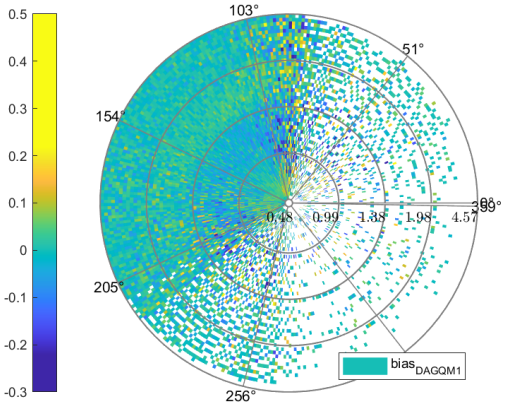

(b) DAGQM1 bias for Gulf of Biscay.

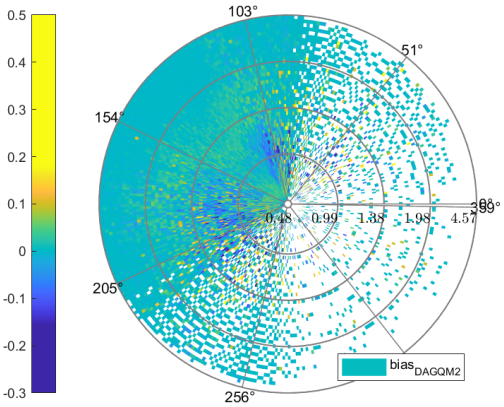

(c) DAGQM2 bias for Gulf of Biscay.

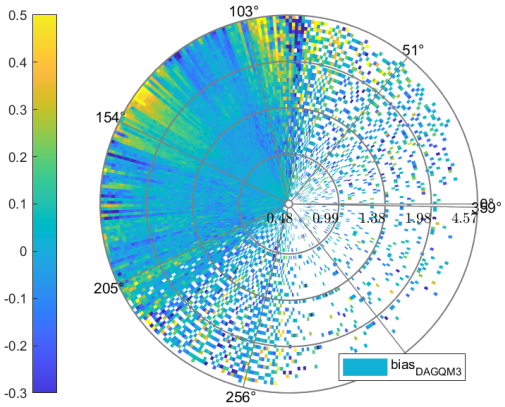

(d) DAGQM3 bias for Gulf of Biscay.

Figure 3.7: Mean bias, per quantile and direction, for each bias correction technique (*Gumbel quantile distribution*).

Again, Figure 3.7d displays, by far, the worst performance among the methods observed, not bringing any directional-based improvement and still showing the highest bias (even higher than the raw simulation, in some extremes). The others, instead, all have in common a better correction of the upper quantiles, while still correcting in a satisfying way the lower and intermediate sea-states (bias almost

never exceeding the 0.1 m threshold, except for very few points). The DAGQM2 technique, in particular, seems to be the best trade-off between extreme events-characterization and an adequate attention to the most common H_s values.
For a further reference, the statistical parameters introduced in the Section 3.2 are reported in Figure 3.8.

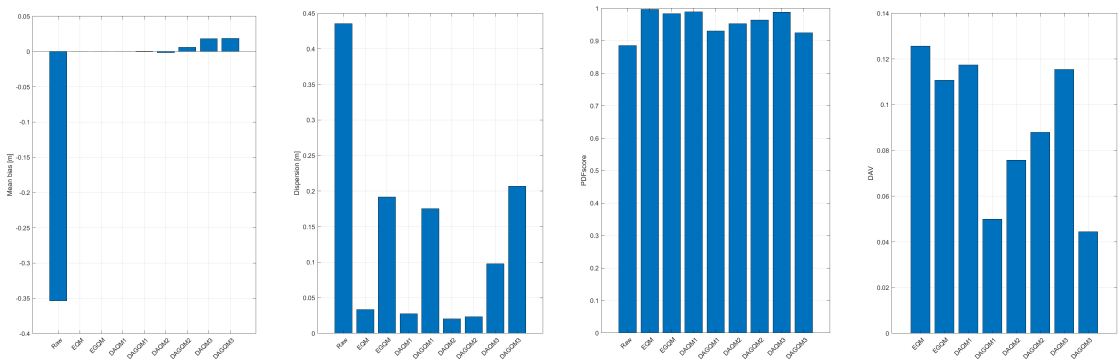

(a) Mean bias. **(b)** Dispersion. **(c)** PDF_{score}. **(d)** DAV.

Figure 3.8: Mean bias, dispersion, PDF_{score} and DAV, per each bias correction technique, for Gulf of Biscay.

Looking at the mean bias, all techniques (even the last two ones, which still perform much worse than the others) significantly reduce the mean bias with respect to raw reanalysis data, going from -0.35 m to a peak of roughly 0.12 m.
Same can be said for dispersion; here, it can be observed that Gumbel-based techniques (with the exception of the previously highlighted DAGQM2) show higher values than the corresponding linear-quantile distribution ones (probably due to a lower attention given to the quantiles below the 99^{th}, that contain the majority of data recorded).
A general improvement characterizes PDF_{score} too, where very little differences are there among correction methods; the DAV, additionally, shows a good improvement for almost all techniques (DAGQM1 and DAGQM3 the worst, by far), with the non-directional methods being among the best.
The fact that the DAQM3 shows a good DAV, without being in accordance with the poor performances highlighted by all other plots and indicators, is explained by keeping in mind that the DAV provides a "general" evaluation about the data distribution as a whole; other metrics such as the polar heatmaps (in Figures 3.6 and 3.7) and the Q-Q plots better seize the "local" deviations, such as those in specific quantiles or directions, which cannot be fully appreciated by a more generic look as the one DAV provides.

Overall, the DAGQM2 seems the most convenient choice, as it offers a good

uncertainty reduction, showing satisfactory overall performances in all plots and indicators, and capturing at the same the most extreme events in terms of wave height without neglecting the other parts of the distribution. Hence, it will be the reference technique for the following parts of the study.
The trends just observed are confirmed in the other locations analysed as well, particularly in Cape Creus and Gulf of Cadiz, where a more diversified wave rose permits to appreciate even more the benefits of the application of directional techniques over the whole wave rose. Following, for the sake of simplicity, the results of the DAGQM2 technique only (the others are available in the Appendix A, for a more complete view of the whole picture) are reported in Figure 3.9.

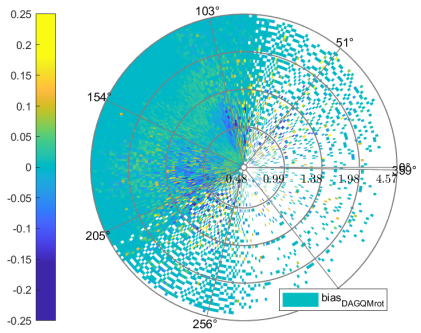

(a) Gulf of Biscay.

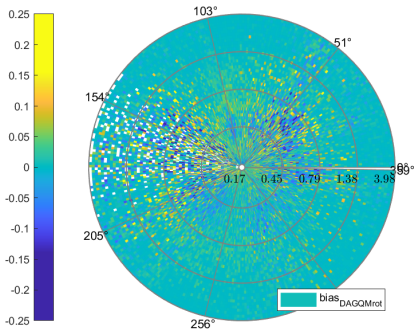

(b) Cape Creus.

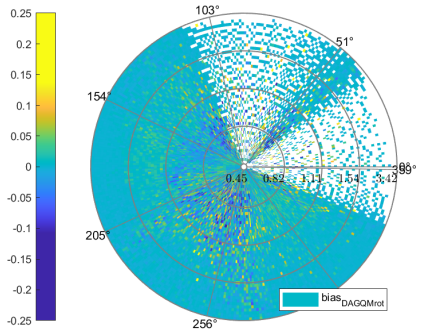

(c) Gulf of Cadiz.

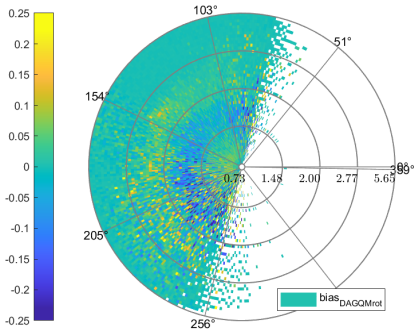

(d) Cape Silleiro.

Figure 3.9: Mean bias, per quantile and direction, for DAGQM2 bias correction technique (comparison among the four locations).

Chapter 4

Bias correction sensitivity

Trials led in Chapter 3 indicated DAGQM2 as the most convenient technique, balancing bias correction quality, statistical indicators and ability to efficiently cover every direction and region of the distribution.
In the energy field application, as large datasets (and, therefore, measurements) are needed [5] [6] for a proper design of offshore facilities, the data gathering process can become very long; running those recordings via current observation devices can be problematic, as their use can get expensive, and they are always exposed to failures and the risk to have periods with relevant lack of data. Reanalysis tools are always available, but without data to compute the correction factors to apply the just described techniques, it is difficult to correct and use them in the design process of an *ORE* installation.
To face this issue, the present is the first (to the author's knowledge) to propose the possibility to split the data into two separate time-windows: an *identification period*, whose data (both observed and assimilated) are used to compute the correction factors, and *application period*, whose metocean values are corrected using the factors obtained from the identification window (as explained in Figure 4.1).

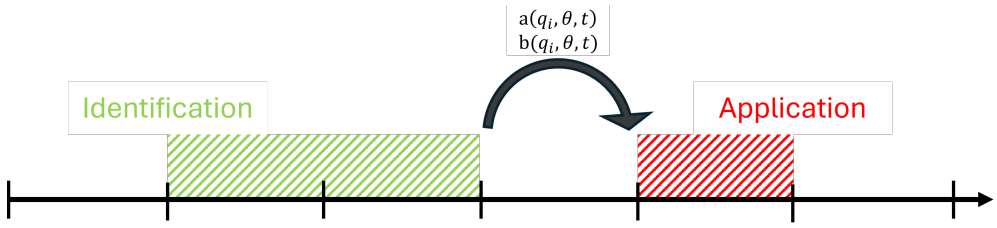

Figure 4.1: *Identification* and *Application* time period representation.

The present study's aim is to establish whether the application of correction factors $a(q_i, \theta, t)$ and $b(q_i, \theta, t)$ obtained in a different time interval than the ones they are used in can still provide with satisfactory and useful data, or if the correction

methods are too affected by this time discrepancy.
Data from upcoming years are in fact crucial in the design process of to-be-installed offshore facilities, to efficiently assess the productivity of a power plant or to plan any maintenance operation on already existing ones. As, of course, observation data from future periods are not available, the study has been led considering in-situ values until the year 2023, accordingly choosing past enough identification windows, in order to still refer to a future time window with respect to the one correction factors are obtained from.
As following sections will present, the analysis has been taken further; an additional, in fact, has been made trying to look for an optimal time period to eventually use for this time-affected correction factors. This part focuses on two points particularly:

- *duration*, meant as the ideal number of years of data that maximizes the accuracy of the bias correction techniques, and

- *instant*, meant as the exact years chosen for the factors' identification.

Following, this study has been conducted, divided in two phases; a *Static Identification Window* one, where the ideal number of years has been investigated, and later a *Moving Identification Window* one, where the "*instant*" component has been added by shifting the identification window chosen.

4.1 Sensitivity Framework

As already anticipated, the analysis has been carried out referring to the DAGQM2 technique only.
Similarly to what previously done, the *mean bias* of the temporally-affected corrected values has been computed. In addition, the ratio between the latter dataset and the one "normally obtained" with present-referred correction factors has been looked at, as:

$$ratio = \frac{y_{sim}^{BC,t}}{y_{sim}^{BC}}, \tag{4.1}$$

where $y_{sim}^{BC,t}$ is the newly considered dataset and y_{sim}^{BC} indicates the first obtained one. This can be useful, as it tells how far the temporally-adjusted correction is from the normal one, and allows to assess whether, in that case, a correlation can be found in terms of eventual under/overestimation per direction and/or quantile.
To, here as well, perform a cross-validation that avoids to run in the occurrence of a single-case where techniques turn out to be effective, the process considers and applies the techniques' results in two different application windows, both five years long: the first from 2015 to 2019, the second from 2019 to 2023.

4.1.1 Static Identification Window

The first part of the temporal sensitivity analysis is divided in two steps: first, the whole 10-years long identification window is considered (from 2000 to 2010); correction factors are obtained from it and applied to the target application periods, as Figure 4.1 explains. Per each quantile and direction, in the form of a heatmap (as done in Chapter 3), mean bias (computed with respect to the application window's data) will be computed and shown, along with the *ratio* introduced in the previous section. These allow to evaluate the correction capabilities of such time-shifted reference data, and provide a visual comparison of how far the results would be from those obtained in the case of a "traditional" calibration method.
After this, the *duration* investigation begins. Within the already introduced 10-year long time window, the identification period is gradually adjusted: starting from 1-year of data (used for correction factors' calculation), the time window is increased one year at a time, results calculated and stored in each of them. In this context, two approaches have been pursued, referred to as "*forwards*" and "*backwards*" analysis (illustrated in Figure 4.2).

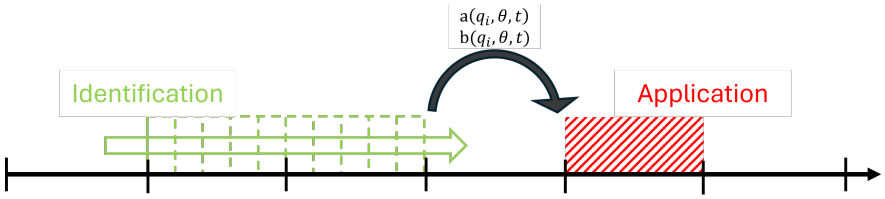

(a) Forwards analysis scheme.

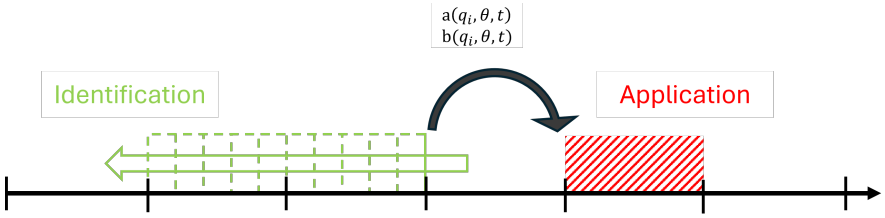

(b) Backwards analysis scheme.

Figure 4.2: Illustration of forwards and backwards analysis time scheme.

In the former, the first year considered for the analysis is the 2000, and the time window is expanded getting progressively closer to the application one; in the latter, the analysis is begun from the last year (2010, for instance, the closest to the application period considered), and the window is enlarged getting progressively further from the 2015-2019 and 2019-2023 windows, as more id. years are included time by time.

This process adds one more layer to the ideal *duration* search, as it allows to investigate whether an ideal amount of years is the same indiscriminately, or depends on the position of the the time window itself (basically anticipating the *instant* issue faced in the following section).
Results here will be mainly shown in a graphic way, via the so-called *boxplots* and *violinplots*. The first provide a visual information about the bias distribution of each obtained dataset and its dispersion (the wider the box is, the more "dispersed" the biases will be). Violinplots, even more explicitly, represent the bias distribution per each number of *identification years* (I.Y.) considered.

4.1.2 Moving Identification Window

After this first part, the ideal *instant*'s assessment has been led. In order to evaluate whether different identification time periods could lead to different results in the bias correction or not, a 10-years long window has been considered, and shifted one year at a time, as much as the data available for each location would allow to. Per each window, the same analysis explained in Section 4.1.1 has been led, defining (within each 10-year reference) multiple identification windows (id. windows), with varying length (Figure 4.3 represents it, for a clearer understanding of the operating procedure). Following this method, it was possible to obtain, for each number of I.Y., several values per each of the metrics presented in Chapter 3 (mean bias, dispersion, PDF_{score} and DAV). As a result, "clouds" of values, along with their centroids, will be displayed, to assess whether a trend in the calibration method's performances can be recognized as a function of the number of years considered (this way, the seek for both ideal *instant* and *duration* of the identification period is carried out at the same time).

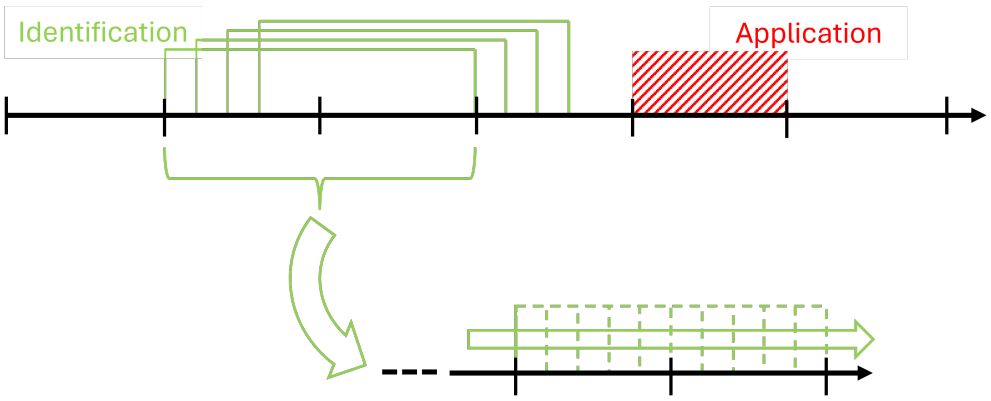

Figure 4.3: Moving Identification Window operating scheme. Many 10-years long periods are defined; for each of them, several periods of increasing length are considered, combining the *instant* and *duration* investigation.

4.2 Sensitivity results

In this section, the results coming from the just explained approaches will be shown. As anticipated, for the Static Identification Window analysis results related to the Gulf of Biscay point only will be reported here, for a matter of space and simplicity; the study has been led for other locations as well, and their outcomes are available in Appendix B. The Moving Identification Window analysis, instead, is fully reported, as the type of visual representation adopted allows to clearly and effectively compare the outputs for each of the sea areas considered.

4.2.1 Static Identification Window results

The first step involved assessing whether correction factors obtained in a past time window than the application one would provide valid results and an effective calibration of the metocean dataset.

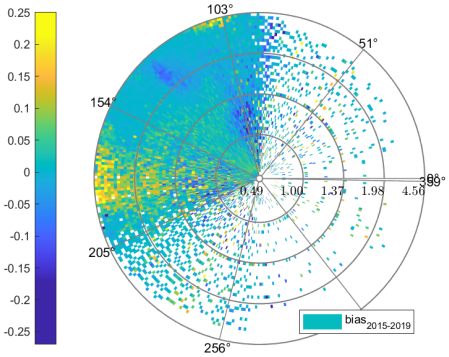

(a) Bias (2015-2019 period).

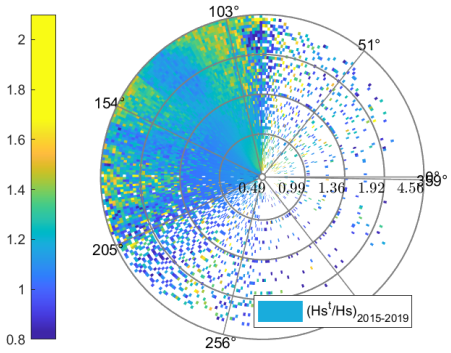

(b) Ratio (2015-2019 period).

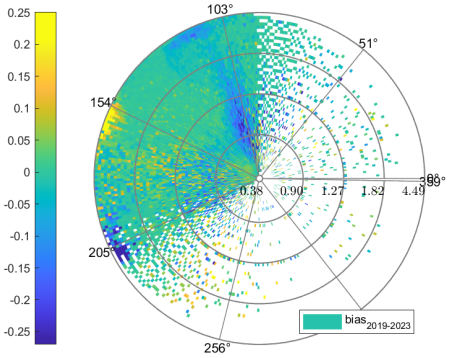

(c) Bias (2019-2023 period).

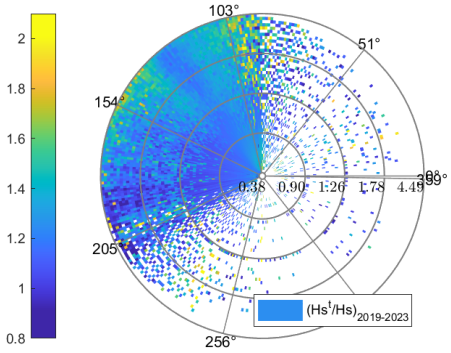

(d) Ratio (2019-2023 period).

Figure 4.4: Per each quantile and direction, bias (on the left) and ratio (on the right) heatmaps (2015-2019 above, 2019-2023 below).

As introduced, for the Gulf of Biscay the evaluation has been made for both 2015-2019 and 2019-2023 application periods. Data from years 2000-2010 has first been taken for correction factors calculation. Figure 4.4 displays the output bias (after calibration) and the ratio between the two calibrated datasets (the time-sensitive and the one obtained via contemporaneous correction factors).
As the pictures show, both application periods observe good correction performances, with bias between -0.05 and 0.05 m in most of the wave rose. Figure 4.4a shows a slight overestimation in the data from the west direction, while in Figure 4.4c a higher bias in the west-northwest and a lower one in the west-southwest are present.
Comparison between these datasets and the ones obtained via a "standard correction", in the form of a ratio, are also displayed in the two heatmaps on the right. Both agree about the two calibrations being consistent, with the ratios rarely going above 1.4. Both display some peaks in some highest quantiles, where the high values of H_s leave margin to higher ratios between the datasets; 2019-2023 application window shows higher maxima, probably due to the time range being further from the identification one. It is also interesting to note how no great consistency is observed in terms of directional behavior of the correction performance, suggesting that, as the periods (and, therefore, the wave distribution) considered are different, the correction factors affect the same directional sector differently in the two cases. Overall, the calibration provided by the correction methods in both cases can be considered satisfactory, and therefore constitutes a good basis to go on with the analysis.

Acknowledging that the correction factors from a certain identification period can be used to correct future values of metocean data with a good enough accuracy, the impact of the number of years considered (ideal *duration* assessment) is investigated. With reference to the Gulf of Biscay, the already introduced framework results, with respect to the 2000-2010 period, in many increasingly long (from 1 to 10 years) identification windows. The process has been repeated following both a *forwards* and a *backwards* approach, to verify whether getting either closer or further to the application period when defining the id. windows could eventually affect the results. The bias correction process has been carried out for each of them, and, in order to carry out an effective comparison among the results, boxplots and violinplots have been used.
The boxplots obtained by the means of the apposite Matlab function provide a visualization of some summary statistics of the bias distribution. In each box, the central red mark indicates the median value, while the bottom and top edges refer to the 25^{th} and 75^{th} quantiles respectively: hence, the boxes contain the most likely to occur bias values. The whiskers extend until all the values that are not considered *outliers*: this term refers to all the values whose distance from the boxes'

edges is more than 1.5 times the interquantile range (=distance between 25^{th} and 75^{th} quantiles, equal to the boxes' height). The smaller a box is, and the shorter the whisker+outliers range is, the less sparse the bias distribution is (theoretically, it should mean that the calibration method is able to provide a more consistent correction performance).

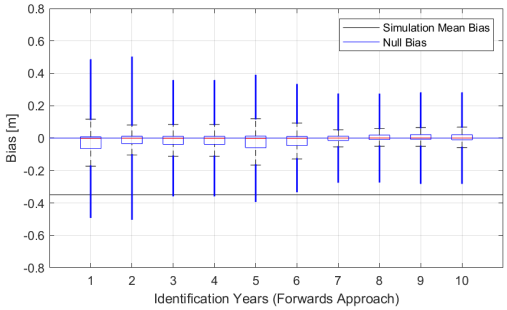

(a) Forward approach, 2015-2019.

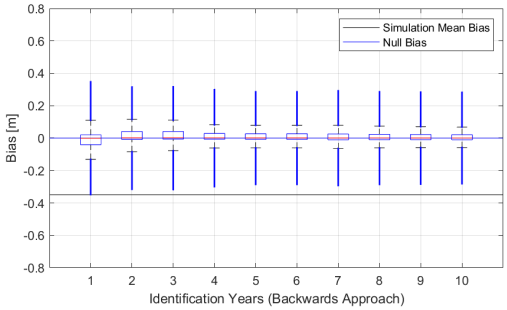

(b) Backwards approach, 2015-2019.

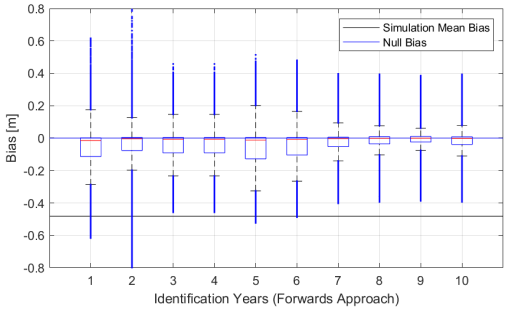

(c) Forwards approach, 2019-2023.

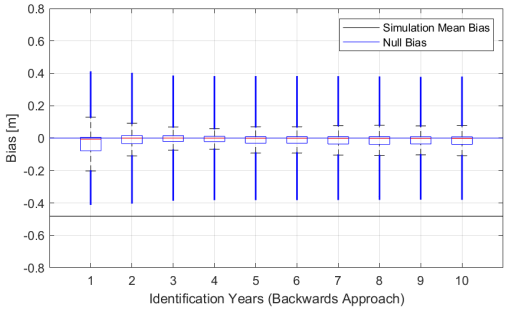

(d) Backwards approach, 2019-2023.

Figure 4.5: Boxplots for both forwards (on the left) and backwards (on the right) identification approach (2015-2019 above, 2019-2023 below).

Looking at the plots, what sticks out immediately is that, the case of a forwards approach, with a 2019-2023 application window, displays by far the highest number of outliers, especially when up to 2 years are used for the identification process. Their quantity considerably reduces when 3 or more years are adopted, and it is necessary to go up to 7 I.Y. to have a more stable (and smaller) boxes' width (from this point on, further increasing does not bring any relevant improvement). A similar trend (even though on a smaller scale) is observed in the forwards approach used for the 2015-2019 application window, where for the first two I.Y. the number of outliers is higher than the rest, and the boxes' width stabilizes from 7 I.Y. on. This suggests that, following this method, the first years, featuring a lower quantity of data for calibration, and being a too far-away time instant from the application

one, do not represent the best data selection option for the techniques' calibration. It is therefore necessary to make sure that, when using such distant data from their reference application instant, a wider dataset has to be adopted.
Additional information is added by the backwards approaches instead, whose trend and results are almost identical (slightly lower bias on the 2015-2019 application window, as expected, being it a few years closer from its identification reference one). Except for the one-year case (whose results are still good, compared to most of the forwards ones), in fact, the outliers' quantity and boxes' length immediately appears small and stable.
A similar information, though in a more explicit way, is provided by the violinplots, where per each number of identification years, the bias distribution is projected (in a shape that recalls a violin, hence the name of this type of graph). Figure 4.6 shows them, with the same disposition adopted for the boxplots.

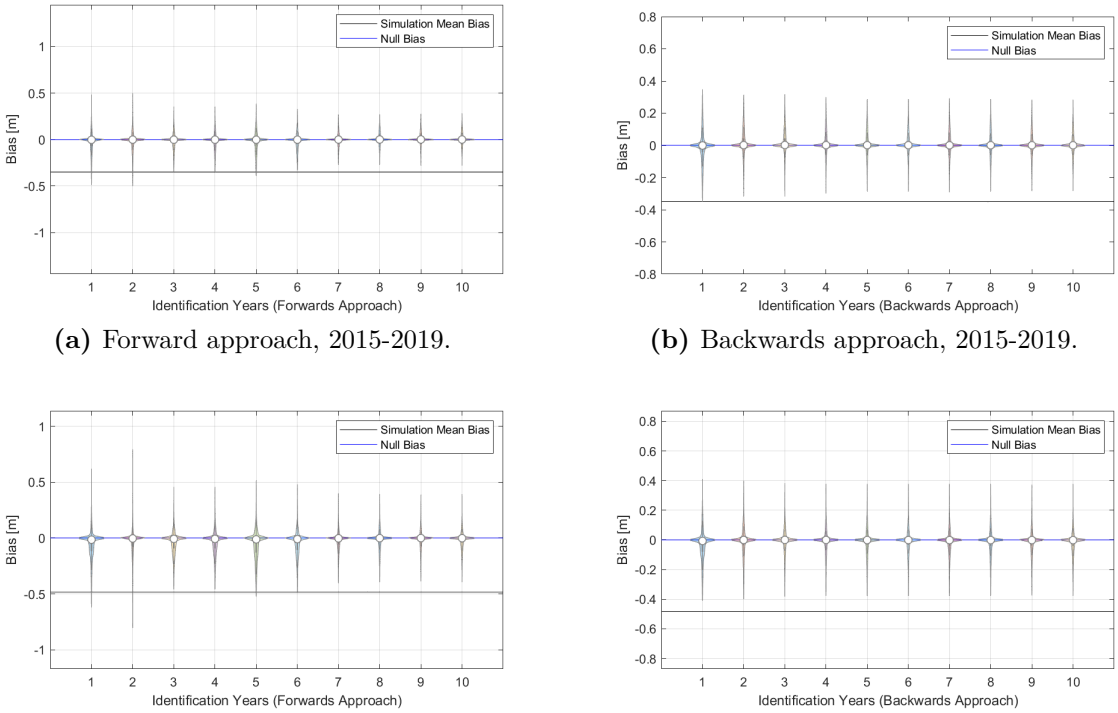

(a) Forward approach, 2015-2019.

(b) Backwards approach, 2015-2019.

(c) Forwards approach, 2019-2023.

(d) Backwards approach, 2019-2023.

Figure 4.6: Violinplots for both forwards (on the left) and backwards (on the right) identification approach (2015-2019 above, 2019-2023 below).

The representation of the bias distribution offers a more direct and explicit visualization of the bias correction techniques' results. First, the fact that all the violins display a thin distribution, with an evident peak around the null bias, indicates

how the uncertainty reduction is effectively carried out in all the cases considered. A comparison among them, on the other hand, confirms what already pointed out via the boxplots. The outliers, in fact, represent nothing more than the distribution tails, which appear much longer for the first plots of the forwards approaches, to then stabilize from 7 I.Y. on. The boxes' width stabilization, additionally, can be observed looking at the difference, (in the 1 I.Y. case for the backwards approach, from 7 I.Y. on in the case of the forwards ones) as the distribution only starts displaying the peak around the 0 bias, while the thicker parts around it disappear where the boxes in Figure 4.5 get smaller.
It is therefore confirmed that, when possible, using data from a period close to the application one is preferred; when further windows need to be used, the analysis recommends considering a long enough (7 years, as highlighted in this case) reference dataset for accurate results. For the outcomes related to the other three locations, the reader is sent to Appendix B.

4.2.2 Moving Identification Window results

After having estimated the ideal duration for the identification window, one more layer has been added to the study, *moving* the id. period itself to search for the ideal time *instant* (and, eventually, check if it actually exists), and observe whether different time ranges can somehow affect the results just observed for the Static Identification Window case.
The adopted framework has already been described in Figure 4.3; according to what the analysis itself allows, no boxplots or violinplots have been produced for this section, as the abundance of information due to the multitude of periods considered would yield an intricate representation. The piece of knowledge provided by the two plots has therefore here been decomposed, as plots about the mean bias, dispersion (both included in the previous representations), PDF_{score} and the DAV have been produced and reported here. The availability of single points (one per each id. period) allows to plot a "cloud of points" per each number of I.Y. (where each point is obtained from a difference reference 10-years-long period). Per each cloud, the centroid (equivalent to the geometric centre of the cloud itself) has been computed, as a mean to outline a trend throughout the increasing number of identification years.
This type of visualization also permits to join the various location in a single plots, finally enabling a clear and immediate comparison among them.
For this analysis, most observation datasets (all, except for the Gulf of Biscay one) didn't go back in time enough to have several 10-year long windows to operate with, if the 2015-2019 window was used; in order to have space for moving the identification period, and end up with clouds displaying enough points, this part of the work has been using with the 2019-2023 application period only. For each

dataset, as many years of data as possible (according to what in-situ measurements provided) have been used; starting from the year 2009 (where a 10-years long window going until 2019 wouldn't have been possible, due to superimposition with the application period), additional 5-years long periods have been considered, to exploit, via smaller identification time ranges, those years too. Specifically:

- For *Gulf of Biscay*, 14 regular windows have been obtained shifting between the 1995-2005 and the 2008-2018 ones. Additional 5-years long windows have been used, moving between the 2009-2014 and the 2013-2018 ones.
- For *Cape Creus*, 7 regular windows have been obtained, moving from the 2002-2012 to the 2008-2018 ones. Additional 5-years long windows used here as well.
- For *Gulf of Cadiz*, 9 regular windows (from 2000-2010 to 2008-2018) have been obtained. Same here for the additional 5-years long ones.
- For *Cape Silleiro*, 9 regular windows (just as before, from 2000-2010 to 2008-2018) too. Same 5-years long additional ones.

The more number of windows available, the more number of points obtained per each cloud (referred to a single location). Below, the result of the analysis per each of the four already introduced metrics are reported.
Figure 4.7 shows the evolution of the mean bias, for both a forwards (above) and a backwards (below) approach. Looking at the centroids, it is immediately clear that, except for Cape Creus (whose mean bias is almost constant, independently from the number of I.Y.), all locations display an increasing trend until 5 I.Y., followed by an evident decrease as the sixth year is included in each identification window; after that, the bias starts increasing again. This is positive for Cape Silleiro and Gulf of Cadiz, as they show a mean bias higher than zero: hence, 6^{th} year's inclusion represents an optimum in their analysis. In the case of Gulf of Biscay, on the other hand, whose mean bias is always negative, 5 identification years seems to be the best choice, as they provide the value closest to zero.
When using a forward approach, then, an intermediate number of I.Y. (between 5 and 6, depending on the case, out of a 10-years long window) seems to be the best compromise, also keeping in mind that, according to the boxplots in 4.5, relevant improvements are hardly observed when 7 or more years are considered, suggesting that too long identification periods are not worth it.
Centroids aside, an important piece of information comes from the clouds of points themselves. It is to be noted, in fact, that although the centroids' trend appears clear and firm, the points' distribution appears to be very sparse in the left part of the plot, suggesting that when few years are considered (moreover, being most of them so far from the application period), correction performances provided by

each window are likely to be very different among each other. Acknowledging this, a number of I.Y. lower than, at least, 4 (that is when the trend stabilizes itself, starting to provide more consistent results) is strongly discouraged, as it is impossible to prior establish whether the data calibration will be good or not.

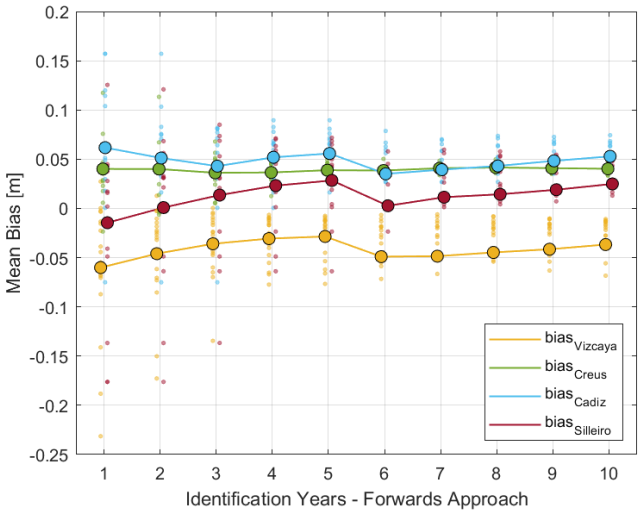

(a) Mean bias trend, forwards approach.

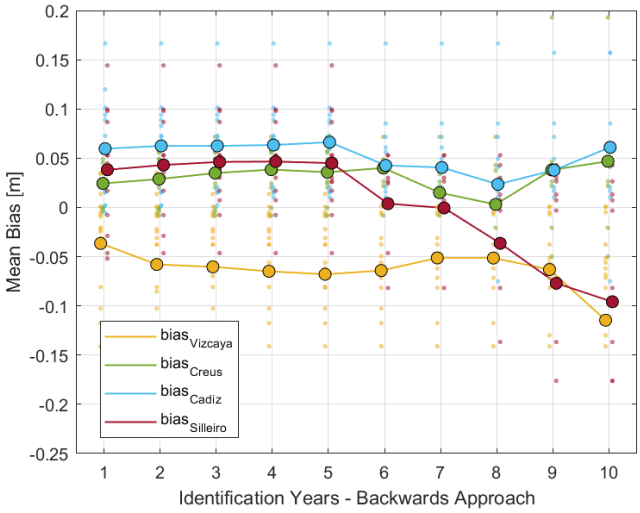

(b) Mean bias trend, backwards approach.

Figure 4.7: Mean bias trend, as a function of the number of Identification Years; forwards approach shown above, backwards approach below (all four locations are compared).

Things are different if the backwards approach is considered, both in terms of centroids' trend and clouds distribution. Starting from the latter, differences can be seen among the locations: Gulf of Biscay and Gulf of Cadiz keep displaying a very sparse point distribution, regardless of the number of I.Y. adopted.; Cape Creus and Cape Silleiro, on the other hand, do show an improvement in terms of results' consistency, as more identification years are used.
Looking at the centroids' overall trend, instead, all locations agree on one thing: as the number of I.Y. gets too high (being in the backwards case, it means that years too far from the application window are included), approaching 9 or 10, correction performances worsen, moving away from the null bias. The individual trends differ from each other though: Cape Silleiro's bias is constantly decreasing (starting from a positive value), Cape Creus and Cape Cadiz agree on showing a minimum (positive) around 8 years, after which it starts increasing again; it is even different for Gulf of Biscay (whose mean bias always maintains lower than zero), where bias decreases until 6 I.Y., to then rise again until 8 years (an optimum here too), and then worsen, in accordance with all the others, as 9 and 10 I.Y. are reached.
These contrasting behaviors might be explained that, when using a backwards approach, two factors intervene:

- on one hand, as the number of years increases, a longer period is considered, more data are used. Most windows start having some common data that, combined to a bigger dataset available for calibration, results in an overall higher results' consistency among the windows (hence, overall less sparse clouds, with a peak between 6 and 7 Y.I.);

- on the other hand, a clear drop in performances was observed as 9 and 10 I.Y. were approached. A possible explanation can be that, increasing the number of identification years here means getting further from the application window, therefore including years that might display very different metocean characteristics from the target ones. It is not to be excluded, though, that the cause might be a problem in those specific years (9 and 10 in the backwards approach, 1 and 2 in the forwards one).

Combining the two approaches, 6-7 years are suggested for correction factors identification, as they are the ideal trade off between a good mean bias (which, for most cases, does not exceed the -0.1/0.1 m range) and a fairly concentrated data cloud. No significant correlations are observed between the calibration's efficiency behavior and the locations' different wave roses and distribution. In Figure 4.7a, the two locations more exposed to the Atlantic's ocean swell waves (Cape Silleiro and Gulf of Biscay) present the same trend, while the others have an overall more stable behavior. Figure 4.7b, instead, immediately appears more chaotic, with no discernible pattern whatsoever. Therefore, it is to be concluded that this analysis

does not reveal the ideal number of I.Y (nor the exact instant) to be directly affected by the location used.

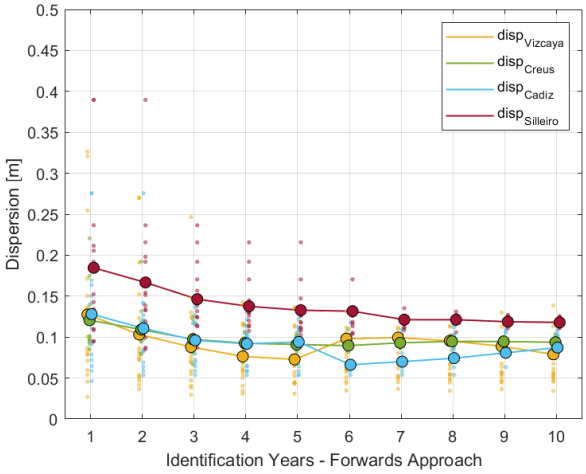

(a) Dispersion trend, forwards approach.

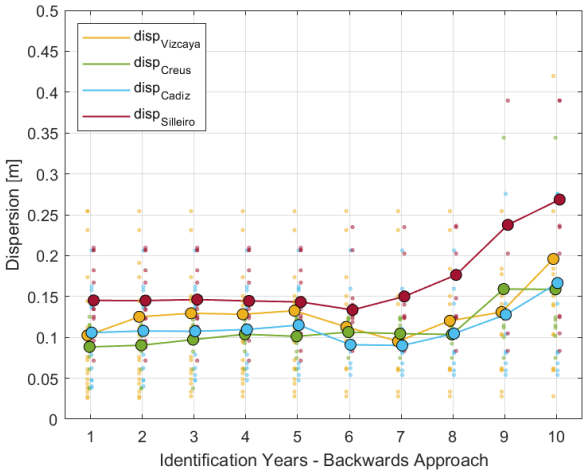

(b) Dispersion trend, backwards approach.

Figure 4.8: Dispersion trend, as a function of the number of Identification Years; forwards approach shown above, backwards approach below (all four locations are compared).

Differently from the mean bias, dispersion (shown in Figure 4.8) shows a much more evident trend (as before, forwards approach is shown above, backwards one is below). In Figure 4.8b (representing the backwards approach), in fact, all locations' dispersion show an increasing behavior, with higher dispersion values and more

distributed clouds of points. In the opposite way, in Figure 4.8a all locations show a decreasing behavior, with dispersions (and respective clouds) converging to lower values between 0.05 and 0.15 m as the I.Y. increase. The positive effect of considering longer identification windows results clear: as larger datasets are used, the calibration technique seems to better cover all the areas of the H_s distribution, resulting in a more compact bias distribution and, therefore, lower dispersion.

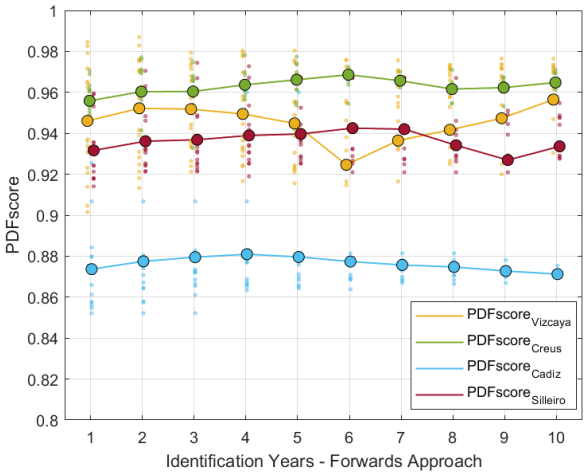

(a) PDF_{score} trend, forwards approach.

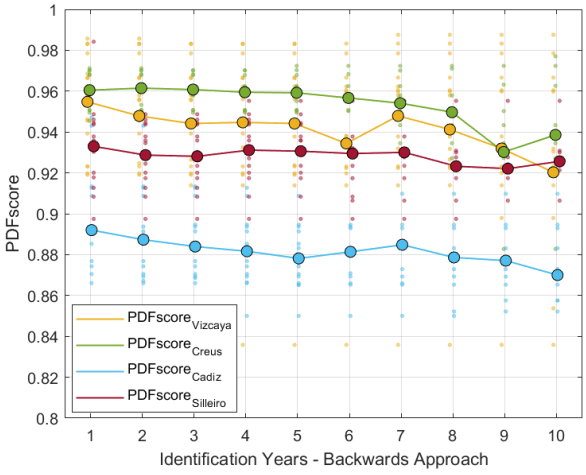

(b) PDF_{score} trend, backwards approach.

Figure 4.9: PDF_{score} trend, as a function of the number of Identification Years; forwards approach shown above, backwards approach below (all four locations are compared).

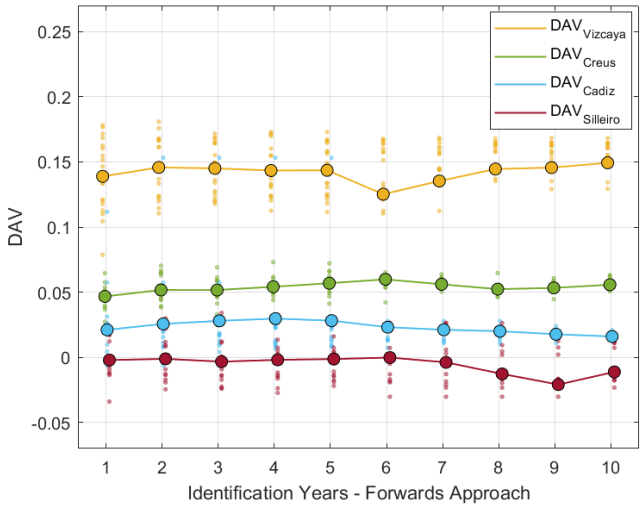

(a) *DAV* trend, forwards approach.

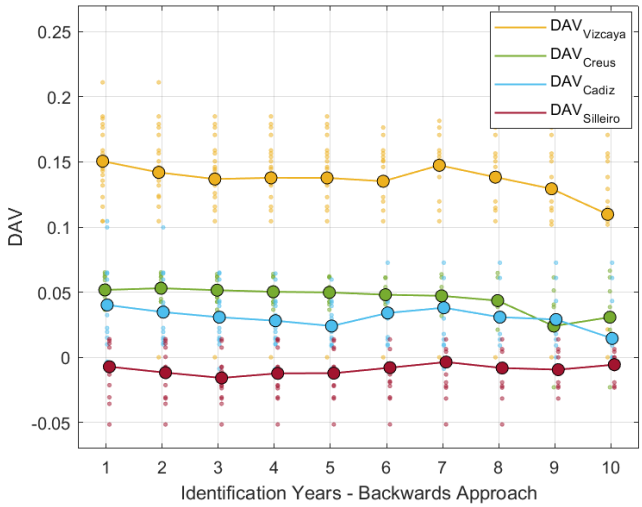

(b) *DAV* trend, backwards approach.

Figure 4.10: *DAV* trend, as a function of the number of Identification Years; forwards approach shown above, backwards approach below (all four locations are compared).

Figures 4.9 and 4.10 focus instead on the PDF_{score} and the *DAV* evolution. Looking at the PDF_{score} first, it sticks out immediately how the lowest calibration performances are observed in Gulf of Cadiz (slightly higher in the backwards case);

it does not surprise, if considered that the same location was characterized by the highest mean bias in both plots in Figure 4.7. The values are overall high in both approaches, and the same cloud's sparseness considerations done before (they tend to concentrate as Y.I. increase, in the forwards case, and to get more distributed in the backwards one) can be seen here. While some kind of trend can be identified in Figure 4.9b, with PDF_{score} decreasing with Y.I. (in accordance to the considerations made before), the same cannot be said for the forwards approach. Here, in fact, all distributions behave differently: Cape Creus and Cape Silleiro seem to show a slightly increasing pattern, the opposite of Gulf of Cadiz (where PDF_{score} seems to get lower as the number of I.Y. gets higher). Gulf of Biscay, on the other hand, appears more irregular, decreasing until 6 I.Y., to then slightly increase and go back continuing its decline (for instance, the same unstable pattern was observed in Figure 4.9a, with Gulf of Biscay being the only one showing an evident minimum for $I.Y. = 6$).

The DAV shows some slightly different information. In both Figures 4.10a and 4.10b, the DAV patterns show great consistency with the ones observed for the PDF_{score} (as their mathematical definition suggests, being the DAV directly related to it); the values associated to each location differ though. Cape Silleiro is, in fact, the one with lowest DAV, while Gulf of Biscay appears to be the one with the biggest improvement brought by calibration, with respect to the raw simulation dataset. Here again, it is hard to observe any relationship with the wave height distributions or the predominant sea-states that characterize the analysed locations.

Summing up the outcomes, the comparative analysis showed that the *DAGQM2* bias correction technique effectively works in all the four locations analysed, and that the results show the margins for some flexibility in the choice of the time windows for identification and application of the correction factors. Although with some obvious differences, both forwards and backwards approaches highlighted the presence of an ideal number of I.Y. (a minimum of 6-7 for the first, while 6 years are just enough in the second case) as a result of a trade off, able to guarantee a solid mean bias (which has been in fact provided in all cases), a good dispersion and pondering what the PDF_{score} and DAV statistical indicators told as well. As all their values turned out to be very good, the distribution of the clouds of point became very relevant, as a minimum number of years to be adopted proved to be able to guarantee consistency in the calibration results, regardless of which window was taken, and therefore setting the user free from the "*instant*'s issue".
In the following section, one more insight has been made, trying to assess whether the sensitivity analysis can be carried out on a seasonal scale, observing eventual variations within the same single identification year.

4.2.3 Seasonal sensitivity

As already mentioned among the purposes and reasons of this work, the in-situ data gathering process can be complicated, long, and expensive. The ideal duration's investigation itself stems from the necessity of a shorter and effective measurement process, as an attempt to evaluate the feasibility of a more compressed procedure without affecting the calibration process' performance.
In this section, this goal has been taken even further, assessing whether, within a time-range smaller than a single year, it was possible to obtain a reliable enough observation dataset for bias calibration techniques' application. A focus has been put on the difference between each 3-month long period, observing the difference is each of their predominant sea-state, and how they could eventually made them a better suit to tailor the calibration on them.

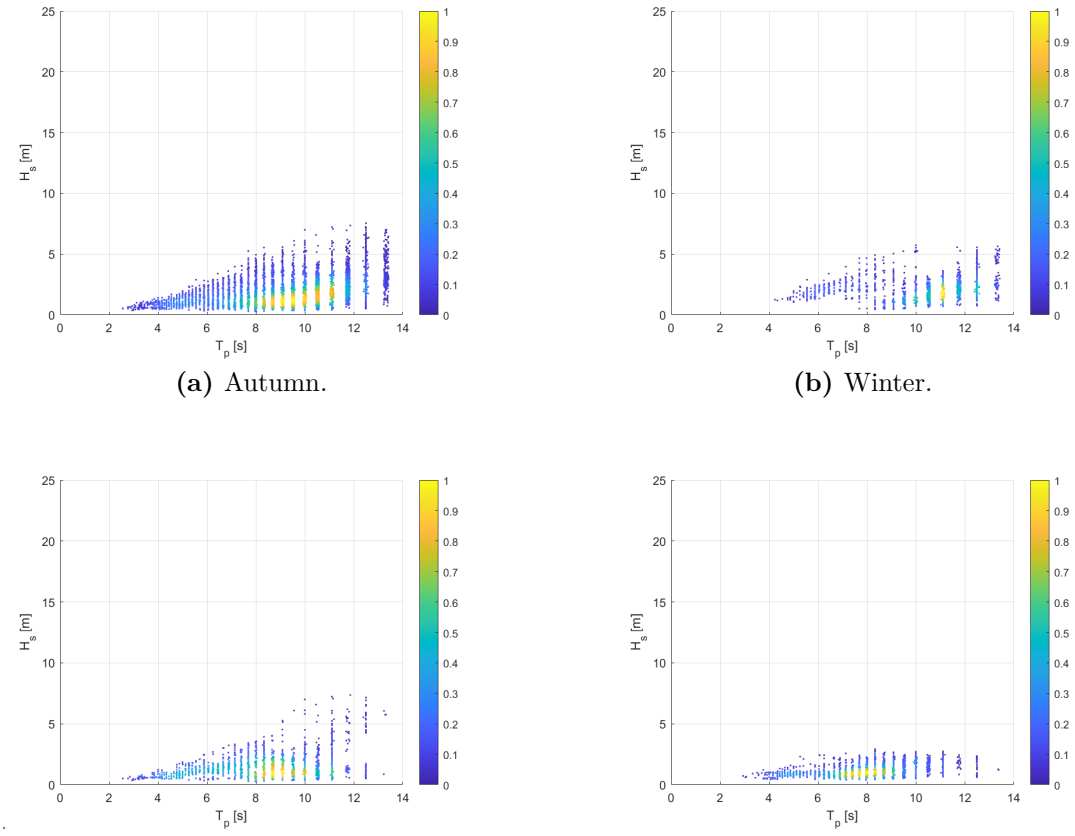

(a) Autumn. **(b)** Winter.

(c) Spring. **(d)** Summer.

Figure 4.11: Occurrence scatter diagrams for each season of the year (Gulf of Biscay, 2012).

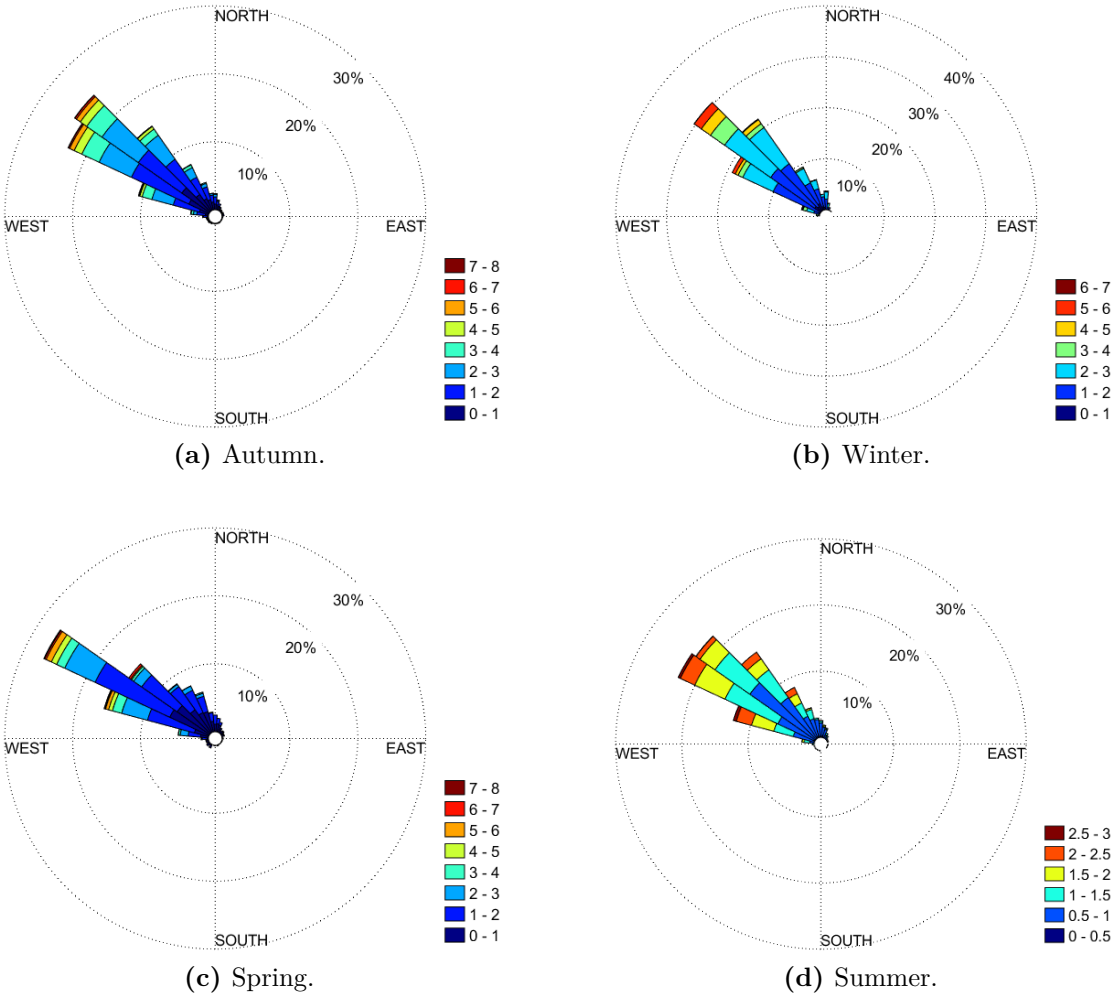

(a) Autumn. **(b)** Winter.

(c) Spring. **(d)** Summer.

Figure 4.12: Wave roses for each season of the year (Gulf of Biscay, 2012).

For the sake of simplicity, only the analysis referred to Gulf of Biscay is reported here; for the other locations and their outcomes, refer to Appendix B. As the identification window has been strongly shortened, and in order to simulate as much as possible a realistic scenario where some years of data have to be corrected, the analysis framework focused on the closest year possible to the application window. According to the data available, 2013-2023 composed the correction window; 2012 has been used for calibration. Figures 4.11 and 4.12 help better characterizing the season dealt with.
In Figure 4.11, the occurrence diagrams for each season of the year 2012 are reported. Each season's climate is perfectly depicted in the occurrence diagram, with autumn covering the widest spectre of wave conditions, followed, as expected, by winter.

Spring and summer, on the other hand, display lower heights and periods, in accordance with a milder weather. Following what displayed here, one could expect that autumn and winter seasons could efficiently provide a better representation of more sea-states, hence more efficiently correcting the dataset throughout all quantiles and directions. Figure 4.12, instead, displays the different wave roses per each season. Summer visibly shows lower values, in accordance with Figure 4.11, suggesting a possible difficulty in covering higher tails of the distribution. All other seasons show a more varied wave rose, in terms of H_s values and direction coverage (spring only shows a slight predominance of western direction).
Given these pieces of information, Figure 4.13 therefore displays the quantile-directions heatmap, where each dot represents the average bias. The scale of each plot has been purposely maintained different, as it was believed very self-explanatory of the difference between each period.

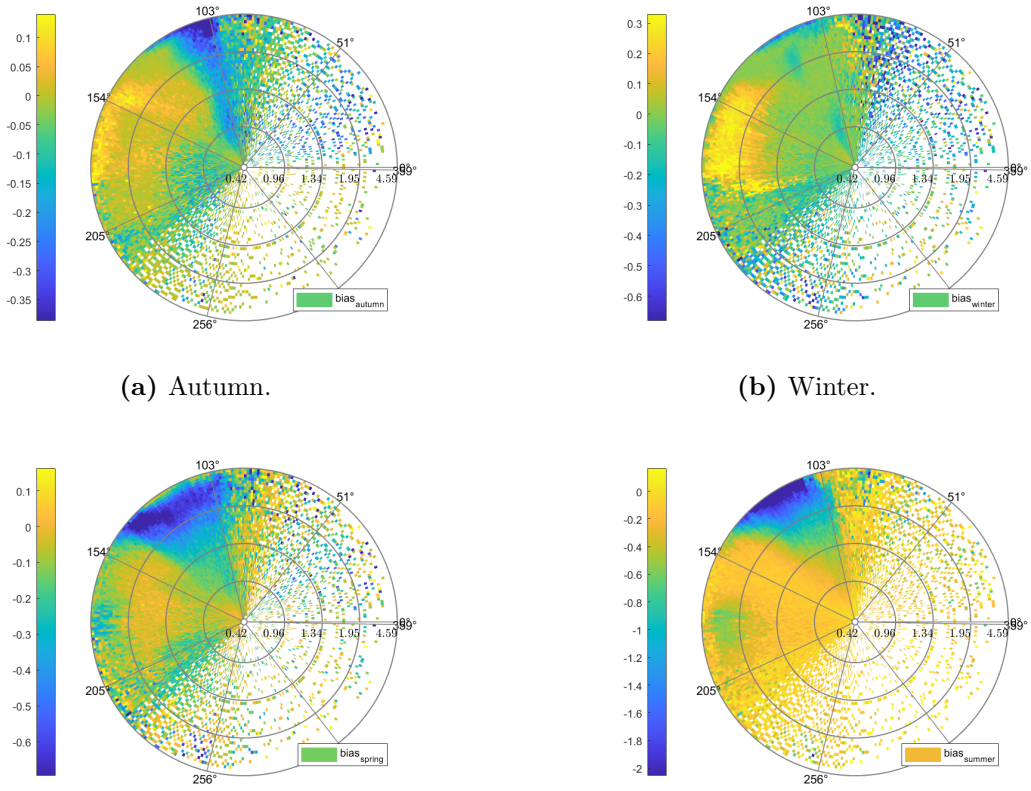

(a) Autumn.

(b) Winter.

(c) Spring.

(d) Summer.

Figure 4.13: Average bias per each quantile and direction in every season of the year (Gulf of Biscay, 2012).

Taking a first look, it immediately sticks out how the season appear to be somehow "paired":

- Spring and summer, in fact, show the same pattern, with an overall good correction in most of the wave rose, but a very strong underestimation of wave heights in the upper quantiles of north-west direction, which, in the summer case, can go down to -2 m. The reason is likely to be searched, as Figure 4.11d points out, in the almost complete lack of high values, with respect to summer (the situation is not very different in spring, with only few waves above 5 m), of H_s for correction factors computation in the upper quantiles of the distribution. This poor availability of data in that region results in a bad ability, of these datasets, to reproduce (and therefore calibrate) some extreme weather regimes, which are crucial when going deep into the design process of a ORE facility, potentially leading to an underestimation of the safety conditions of the energy plant.

- Autumn and winter, on the other hand, share a pattern of light over-correction in the western direction (slightly higher for winter, reaching 0.3 m in some quantiles), but an overall better performance. Winter, in particular, seems the one offering the best compromise, with a better-spread of bias values close to zero (as the green distributed spot in Figure 4.13b suggests). Furthermore, it does not display the same underestimation area in the NW direction (in favour of only a few isolated dots) as the autumn plot does; looking at the circles' reference in Figure 4.12, this might be explained with a more distributed winter spectrum, towards north-west as well, with respect to autumn, eventually causing a slightly worse representation of those waves. Still, the underestimation does not go lower than 0.35 m (absolute value), as a reminder that calibration properties can still be considered satisfactory.

A direct and overall view of the results obtained, enabling an even more effective comparison among seasons, is reported in Figure 4.14. It shows the boxplots referred to each season, for a comparison that enables visualizing dispersion and the median of each obtained datasets. Corrections obtained using the whole 2012 (referred to as "*1 year*") and the present 2013-2023 period (referred to as "*Reference*" in the plot) are displayed as well for comparison.
Summer immediately appears as the worst season by far, with the box never getting to the zero-bias line (the opposite, actually being crossed by the mean simulation one, suggesting very little improvement with respect to the raw dataset) and very long whiskers and abundance of outliers. Spring too displays a large box, representing a high dispersion of data, while autumn and winter distinct themselves as much better options for correction factors identification. Both show low dispersion (autumn actually having less outliers as well) and a median coinciding

with the zero-bias line, although winter's box appears slightly better centred. The present-time reference correction keeps itself out of reach, confirming again, though, the quality of the calibration method and its ability to effectively fix the uncertainty on the assimilated dataset.

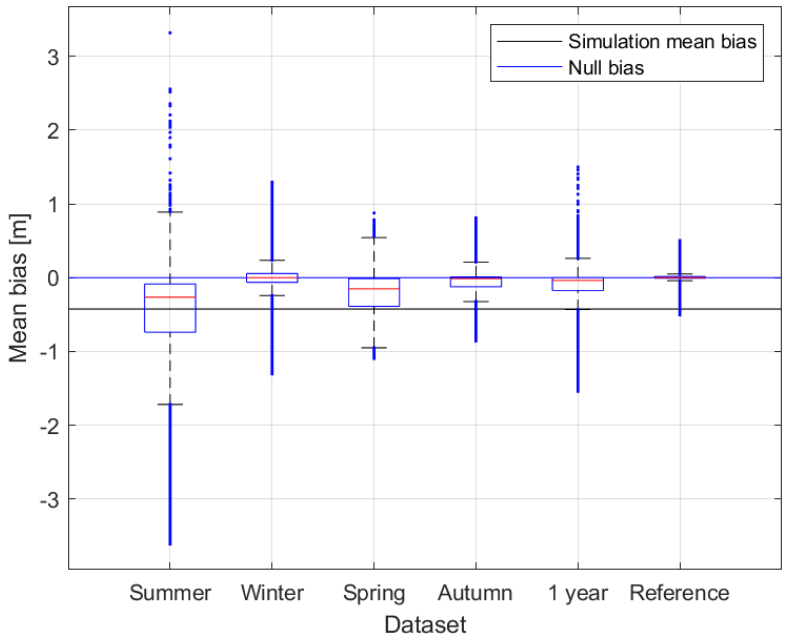

Figure 4.14: Boxplots comparing each season of the year 2012; the whole identification year, and a present-time correction (referred to 2013-2023) have been included as well for comparison.

As already expected, therefore, autumn and winter clearly seem to be the best options if wanting to only use a single season for correction factors identification. Their better spread (in terms of H_s values and directions) wave distribution in fact makes them a better fit to calibrate the correction methods on, effectively covering a 10-year long period successive to the chosen identification year.
Curiously, from the plot is seems that both autumn and winter actually perform better than the case where the whole year 2012 is used for identification. This is actually encouraging, as it tells that reducing the window down to a single season is not only possible, but (in this specific case) can actually allow a better correction process while saving time and money for metocean data gathering through an in-situ observation device. A validation with different time periods has not been performed here, as this would have implied moving out of the scopes of this work and would have made it too intricate to be exposed in these pages; Appendix B.2 performs the same analysis on the other locations considered though, for a cross-validation of the results obtained.

Chapter 5

Conclusions

The present work studied the effect of integrating wave directions in bias correction techniques applied to re-analysis metocean datasets.
The availability of reliable wind and wave information is in fact crucial for the optimal design and maintenance of offshore renewable energy installations and can represent a relevant push in their development, as they can play a leading role in the transition towards a cleaner and more sustainable energy production.

Accounting for wave direction in the calibration methods for H_S values has been proven effective, as results in Section 3.3 show. The outcomes obtained in the Gulf of Biscay analysis (and confirmed by the cross-validation performed with the other locations) seem to agree highlighting Gumbel-based techniques as the most effective (*DAGQM2* especially), as they guarantee a more uniform correction, not neglecting any region of the wave rose nor of the quantile distribution (confirmed and enforced by the dispersion values obtained).
The *DAQM3* technique seems to be the only one not performing as expected. Such wide identification sectors (22.5°) with respect to the smaller (1°) application ones may in fact produce a too big discrepancy in the information collected within the identification process; hence, correction factors obtained this way are not the best fit.
Using different locations, with such different wave roses and sea-states (pure swell waves in the Atlantic Ocean, wind seas in Cape Creus in the Mediterranean Sea, and a mixed climate in Gulf of Cadiz) helped validating the implemented techniques, proving their effectiveness regardless of the area they're applied in and its characteristics, stating their validity and proposing them as a tool for obtaining reliable datasets for the design of offshore energy installations.

The study has been pushed forward: correction factors obtained in a reference 10-years long window were proved to be reliable even in two different future 5-years

long time ranges, showing in both cases their effectiveness even if referred to a different time period than the application one.
Via the static and moving identification window analyses, the study has investigated the *duration* and time *instant* issues. The ideal length and position of the identification period were looked for, and by trying out different periods and comparing their outcomes, it was actually observed that the further the two periods (identification and application) are, the more a longer id. window is suggested: summing up, a 6-7 years long range represents a good trade off, ensuring quite precise and consistent results almost regardless of which instant is used, bypassing the problem and guaranteeing a solid data calibration.
With the aim of saving money and time in the process of observation data gathering, it was also explored if a single season was enough for obtaining correction factors to calibrate the successive ten years. A comparison among each season was carried out, eventually pointing out that autumn, experiencing the highest variety of wave conditions, was actually able to cover the spectre of sea-states even better than the whole year-long analysis, providing an effective correction to the selected application period.

As mentioned, directional bias correction techniques proved to be a powerful and reliable instrument. Their application and effects on actual energy installations are yet to be assessed. Following this path, the study presents several possible developments, as future research studies should involve:

- Assessing the impact of the implemented bias correction techniques on *ORE*'s design process, using specific *ORE* design parameters;
- Exploring the possibility of using other datasets (*i.e.* satellite-based ones) as a reference for the techniques' calibration where necessary;
- Expanding the work adding one more layer of *spatial sensitivity*, assessing how correction factors' validity preserve itself in different sea-areas than the one they have been identified in; the last two, in particular, would bring an additional and powerful layer to the bias correction process, as it would allow a deeper more accurate knowledge of metocean conditions in areas that, otherwise, would suffer a lack of accurate and reliable information for *ORE*'s installation design.

Appendix A

Bias correction results for all locations

In this Appendix, bias correction results related to the remaining locations are reported, to assess the calibration methods' performances outside of the Gulf of Biscay area, and check if consistency or incongruities are observed within them.
The results' representation will follow the same order as in Section 3.3, to make the comparison easier between the two sections.

A.1 Cape Creus

First on, Cape Creus (in north-western Mediterranean sea) is analysed. Its quantile-quantile plots per each technique are reported in Figure A.1 (whole datasets are considered here; further representations will allow to better observe the differences between the directions).
First results seem to agree with the ones showed for Gulf of Biscay in Figure 3.5, with linear techniques performing well below the 99^{th} quantile (Linear Quantile Mapping being the only one to still be reliable above that threshold; DAQM follows, although not close), but having troubles in capturing most extreme wave events. Gumbel-distribution techniques, on the other hand, all solve this issue very well, once again, without showing losses, in terms of accuracy, in the lower and middle quantiles; no significant differences, from this general sight, are observed between the EGQM and the directional techniques.
The DAQM2rot technique, including an identification and an application sector, keeps being the less performing one, especially as the upper tail of distribution is approached (differently from the others, not even a Gumbel quantile distribution appears able to fix this problem here).

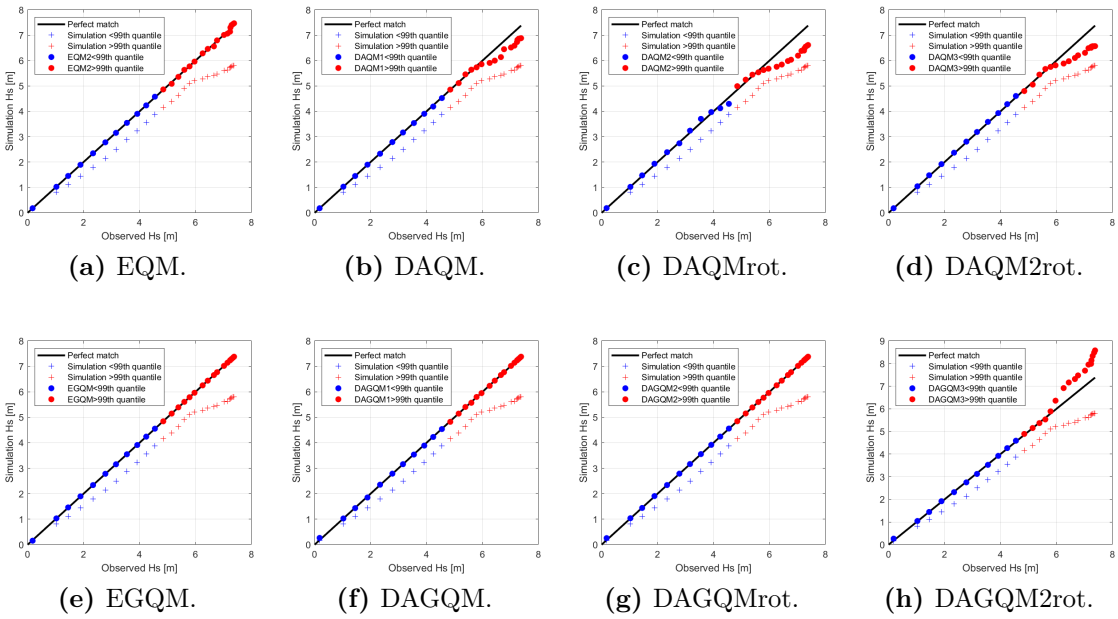

(a) EQM. **(b)** DAQM. **(c)** DAQMrot. **(d)** DAQM2rot.

(e) EGQM. **(f)** DAGQM. **(g)** DAGQMrot. **(h)** DAGQM2rot.

Figure A.1: Q-Q plots for each bias correction technique (*linear* quantile distribution above, *Gumbel* quantile distribution below). The blue and red symbols refers to quantiles below and above the 99^{th}, respectively.

Keeping in mind the difference between the wave roses (showed in Figure 3.3), directional heatmaps are reported as well. While Gulf of Biscay showed a huge predominance of north-western waves, Cape Creus shows a more spread distribution, with a peak coming from north and another (smaller) one for south-west. Although being less, south-eastern waves are present as well.
The simulation bias, represented in Figure 3.4b, highlighted a good representation of the most common wave directions (in the NNW and SW directions), while, on the other hand, higher absolute bias values were recorded in the SSE direction and, most of all, a strong underestimation characterizes the upper quantiles of the directions with less wave data, indicating a difficulty in reproducing extreme events when a scarce information is available. Figures A.2 and A.3 refer to linear and Gumbel quantile distribution techniques' results, respectively. Is is to note that the scale has been purposely maintained different between Figure A.2d and the others, as the latter's bias reaches much higher values.
The first three techniques, in fact, all agree in showing the same trend, characterized by a very effective correction throughout all directions, and a bigger uncertainty (highest bias values actually displayed by the non-directional quantile mapping, although by not too much) in the upper quantiles that interests the same directions as the ones seen when talking about raw simulations' bias.

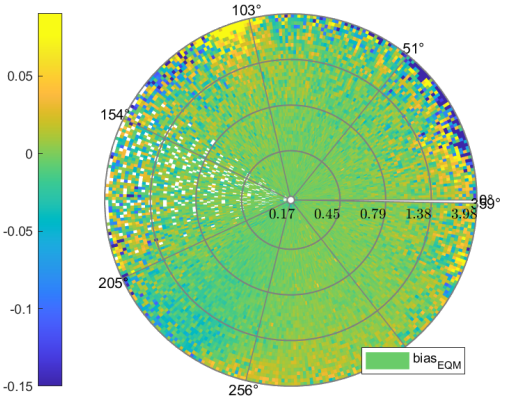

(a) Linear quantile mapping bias for Cape Creus.

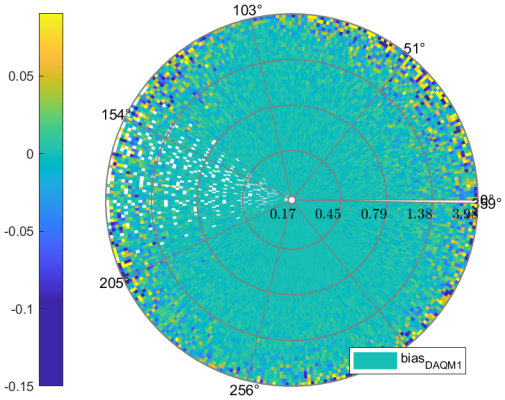

(b) DAQM bias for Cape Creus.

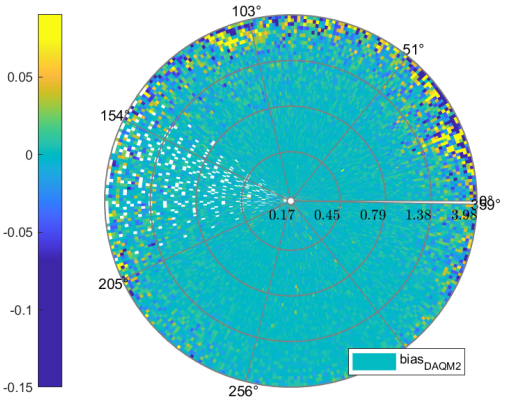

(c) DAQMrot bias for Cape Creus.

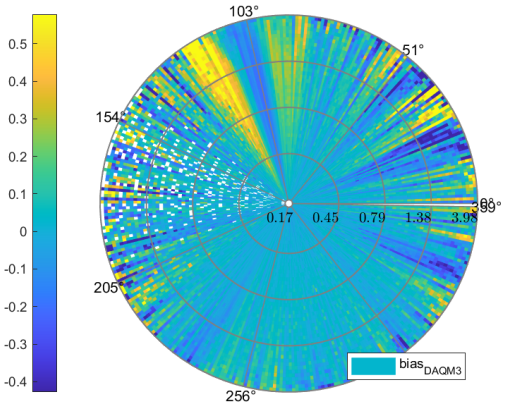

(d) DAQM2rot bias for Cape Creus.

Figure A.2: Mean bias, per quantile and direction, for linear quantile distribution bias correction technique (Cape Creus).

Colour's scale has purposely been kept different for Gumbel distribution's plots: just as in the linear distribution case, the DAGQM2rot's results immediately stick out as much worse than all the others, proving again the unreliability of this method regardless of the quantile distribution adopted. It is interesting to note how non-linear and directional methods show similar scales and commonly-low bias, but a completely different directional pattern: while DAGQM, in fact, reduces the bias to almost zero quite evenly, the EGQM techniques does not seem to display a directional criterion in correction's effectiveness, with some over-estimated spots in north-western and, especially, southern direction. This, even more than in Gulf of

Biscay (whose wave rose was strongly dominated by a single direction), evidences the advantage that directional techniques bring when the directional spectrum is wider, and dedicated calibration processes are necessary. Looking at the colour scale, finally, DAGQMrot turns out to be the most performing method here too, bringing most quantiles' bias down to zero (or very close to it). As a downside, Gumbel distributions techniques obviously lose some accuracy in some lower and intermediate quantiles, although the bias always keeps itself to acceptable values.

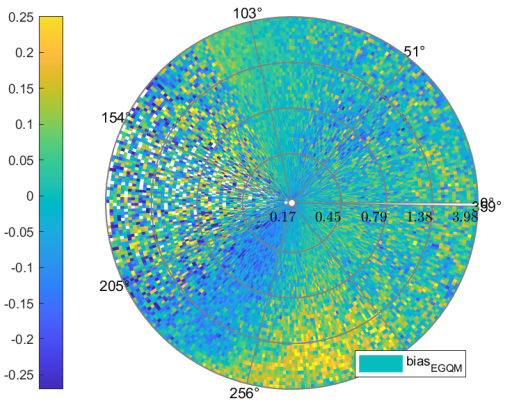

(a) Gumbel quantile mapping bias for Cape Creus.

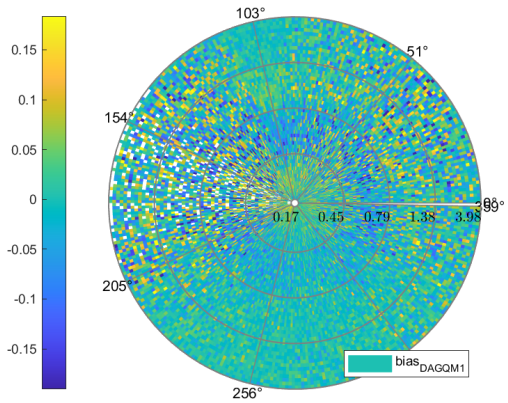

(b) DAGQM bias for Cape Creus.

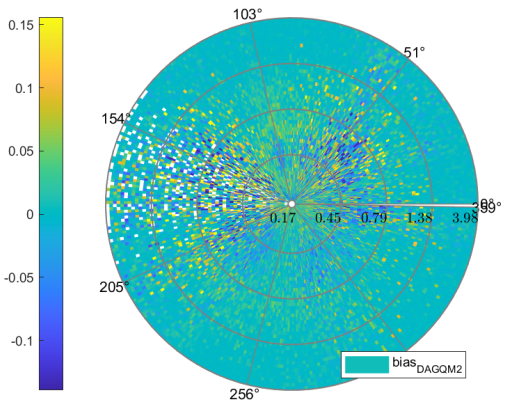

(c) DAGQMrot bias for Cape Creus.

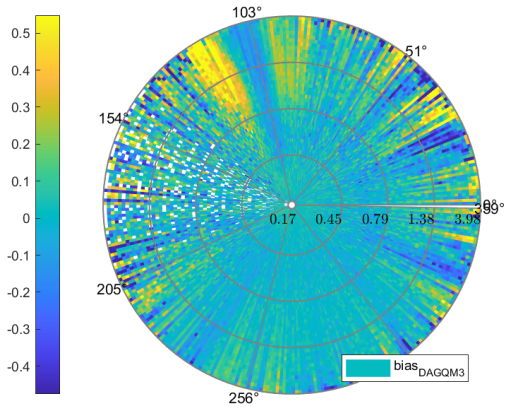

(d) DAGQM2rot bias for Cape Creus.

Figure A.3: Mean bias, per quantile and direction, for Gumbel quantile distribution bias correction technique (Cape Creus).

Finally, statistical metrics are reported in Figure A.4. Each metric shows total accordance to the ones obtained for Gulf of Biscay and displayed in Figure 3.8; all considerations previously applied keep being valid in the same way.

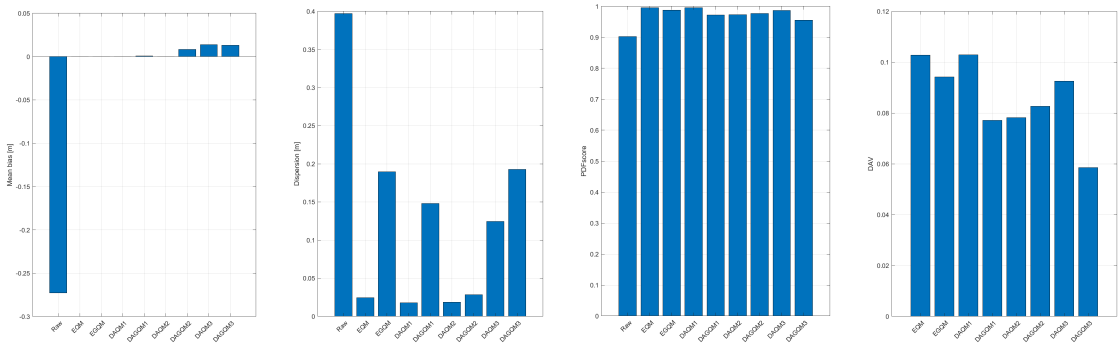

(a) Mean bias. **(b)** Dispersion. **(c)** PDF_{score}. **(d)** DAV.

Figure A.4: Mean bias, dispersion, PDF_{score} and DAV, per each bias correction technique, for Cape Creus.

A.2 Gulf of Cadiz

Results for Gulf of Cadiz are reported, starting from the QQ-plots in Figure A.5.

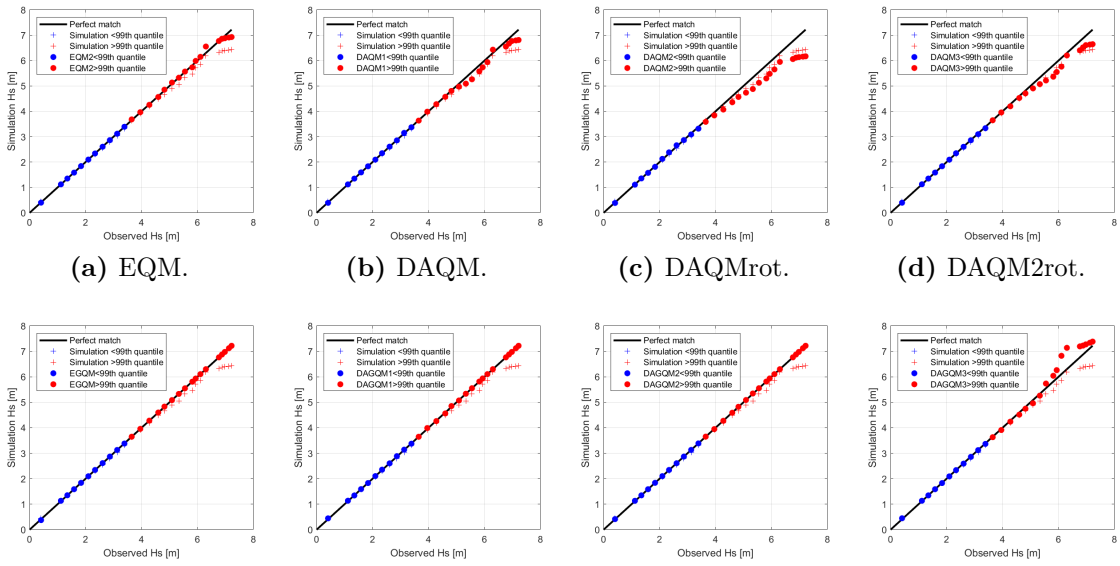

(a) EQM. **(b)** DAQM. **(c)** DAQMrot. **(d)** DAQM2rot.

(e) EGQM. **(f)** DAGQM. **(g)** DAGQMrot. **(h)** DAGQM2rot.

Figure A.5: Q-Q plots for each bias correction technique (*linear* quantile distribution above, *Gumbel* quantile distribution below).

QQplots here too confirm the results obtained in the past two locations (even linear quantile mapping here clearly loses some accuracy in the top quantiles).

Figure A.6 shows the bias heatmaps for linear quantile distribution techniques (to be noted, the scale of DAQM2rot is significantly different from the others). The same trend observed in other locations is confirmed here, with a bias always between -0.1 and 0.1 m, and the same difficulty in capturing higher quantiles' regions.

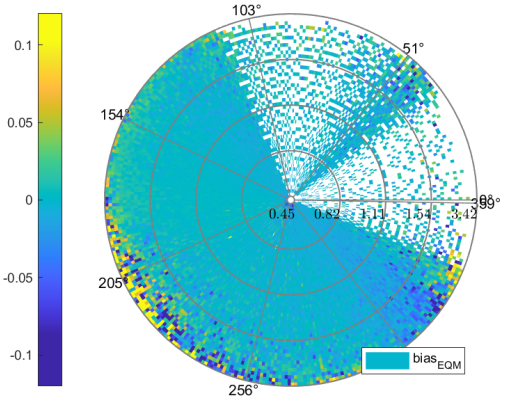

(a) Linear quantile mapping bias for gulf of Cadiz.

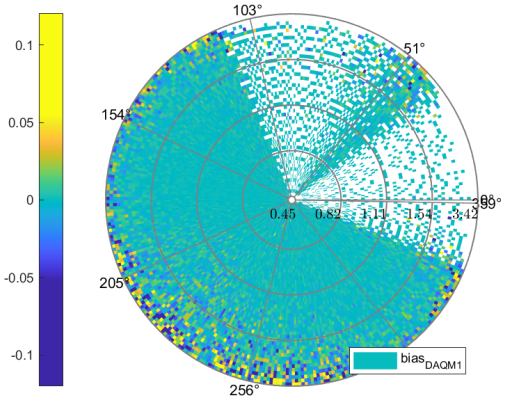

(b) DAQM bias for Gulf of Cadiz.

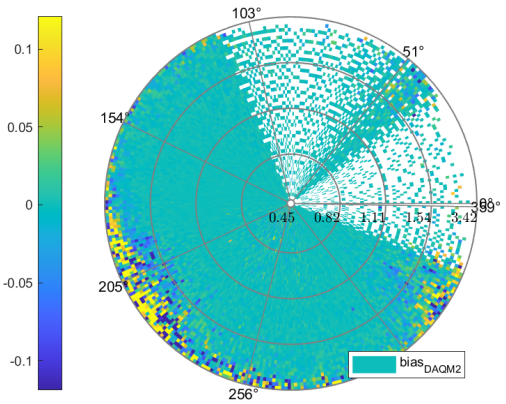

(c) DAQMrot bias for Gulf of Cadiz.

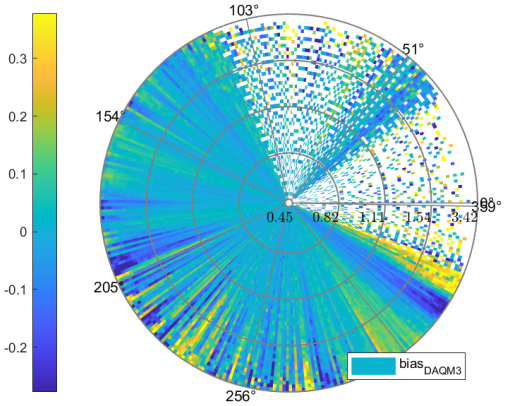

(d) DAQM2rot bias for Gulf of Cadiz.

Figure A.6: Mean bias, per quantile and direction, for linear quantile distribution bias correction technique (Gulf of Cadiz).

Figure A.7, displaying Gumbel distribution techniques, confirms what previous analyses stated; the more even quantile distribution (including a more accurate representation of extreme phenomena) still highlights the DAGQMrot technique as the best one; furthermore, this visualization, again, allows to observe how directional techniques uniformly correct the data along the whole wave rose, while the

non-directional one does not seem to follow any pattern.

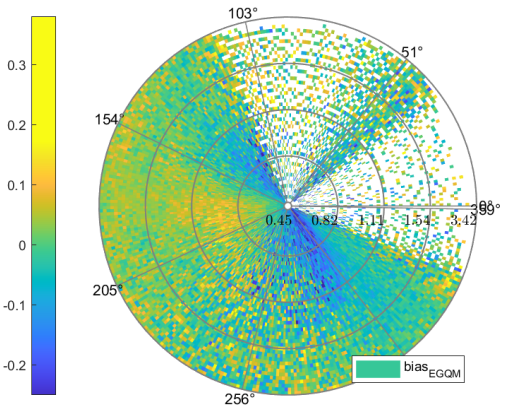

(a) Gumbel quantile mapping bias for gulf of Cadiz.

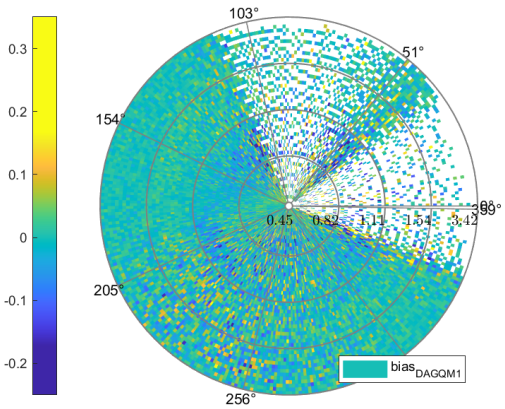

(b) DAGQM bias for Gulf of Cadiz.

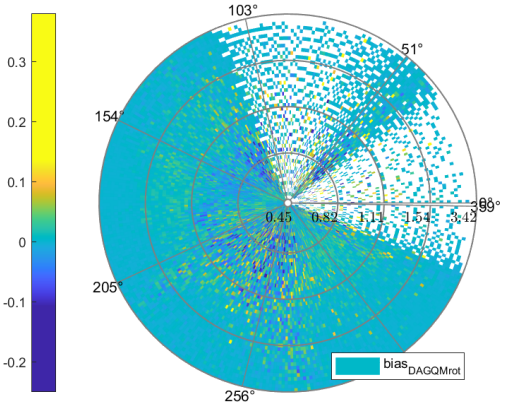

(c) DAGQMrot bias for Gulf of Cadiz.

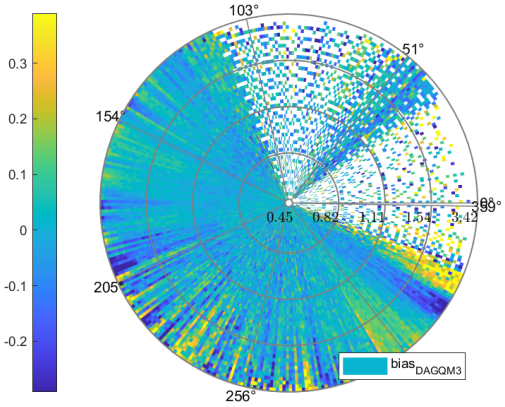

(d) DAGQM2rot bias for Gulf of Cadiz.

Figure A.7: Mean bias, per quantile and direction, for Gumbel quantile distribution bias correction technique (Gulf of Cadiz).

Again, statistical metrics are reported in Figure A.8. Here, DAGQMrot distinguishes as the technique with the highest mean bias (to be specified, it can also be the result of many positive and negative values; still, in the order of 10^{-3}); it also owns a very low dispersion though, indicating a very good consistency in providing a good correction and mean bias. It is to note that this is the only case where DAV is not always positive (down to -0.03).

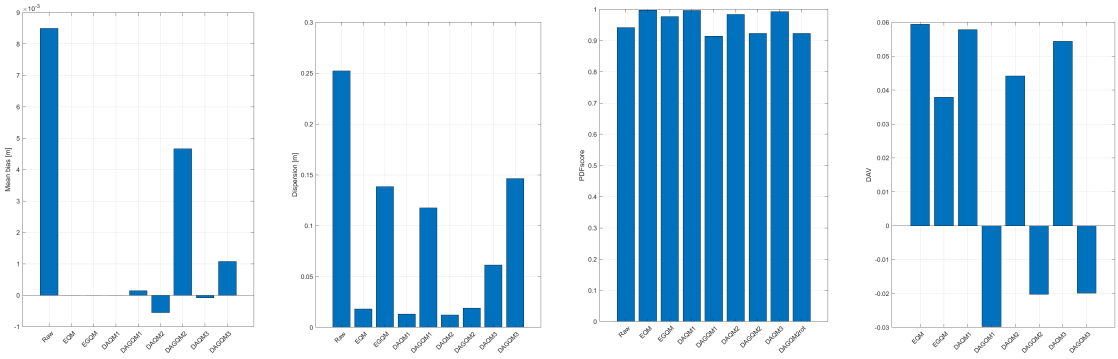

(a) Mean bias. **(b)** Dispersion. **(c)** PDF_{score}. **(d)** DAV.

Figure A.8: Mean bias, dispersion, PDF_{score} and DAV, per each bias correction technique, for Gulf of Cadiz.

A.3 Cape Silleiro

Finally, analysis' results for Cape Silleiro are reported here.

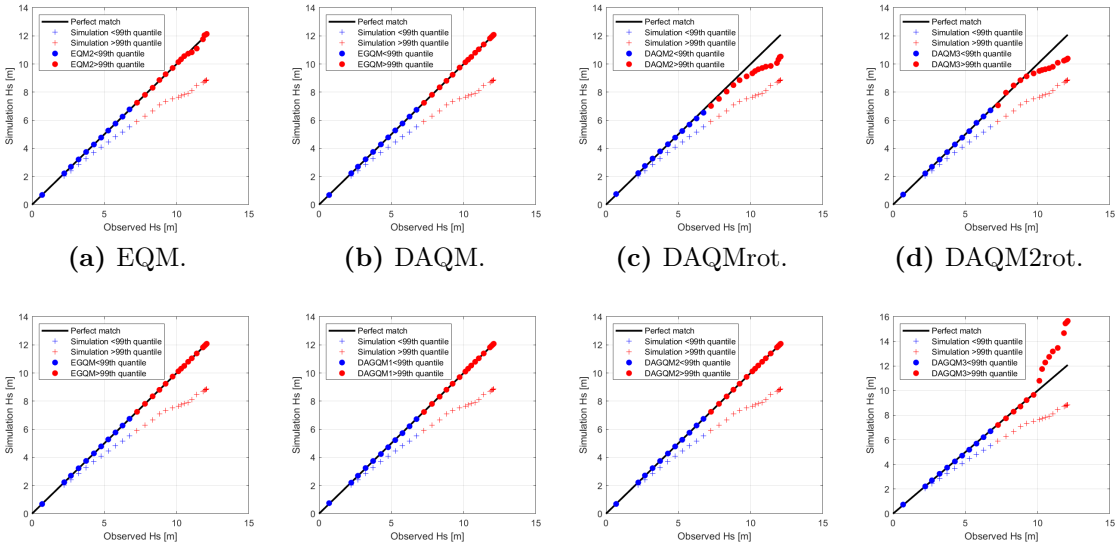

(a) EQM. **(b)** DAQM. **(c)** DAQMrot. **(d)** DAQM2rot.

(e) EGQM. **(f)** DAGQM. **(g)** DAGQMrot. **(h)** DAGQM2rot.

Figure A.9: Q-Q plots for each bias correction technique (*linear* quantile distribution above, *Gumbel* quantile distribution below).

Figure A.9 shows the QQ-plots. This is the case where, more than the others, most linear techniques still cover upper quantiles sufficiently well (linear quantile

mapping actually being the worst here, from this point view). DAQM2rot (and its Gumbel correspondent) still stick out as the worst.
In Figure A.10, mean bias per quantile and direction is reported (scales have purposely been kept different here too). There are some differences between the methods here, as DAQM shows a very small one (between -0.6 and 0.6 m), that gets gradually higher for linear quantile mapping and DAQM (DAQM2rot still being out of reach).

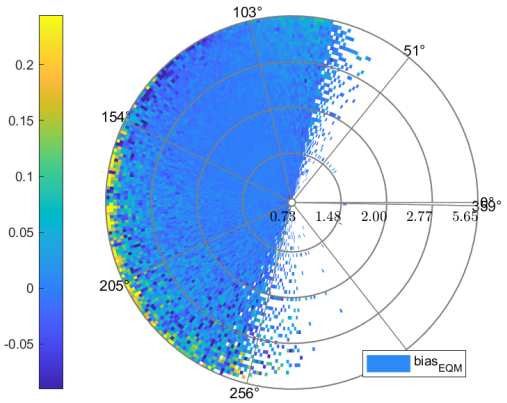

(a) Linear quantile mapping bias for Cape Silleiro.

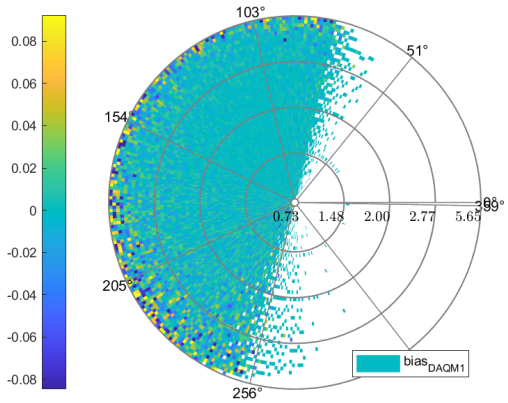

(b) DAQM bias for Cape Silleiro.

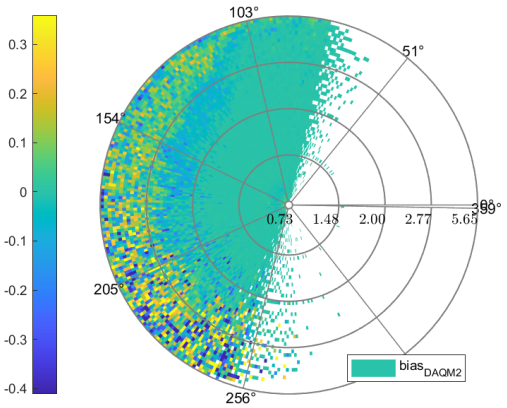

(c) DAQMrot bias for Cape Silleiro.

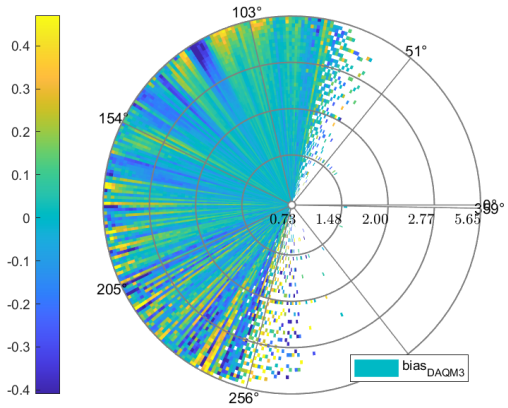

(d) DAQM2rot bias for Cape Silleiro.

Figure A.10: Mean bias, per quantile and direction, for linear quantile distribution bias correction technique (Cape Silleiro).

Switching the focus on Figure A.11, referring now to Gumbel-based techniques, the results show good consistency with what already observed in the previous

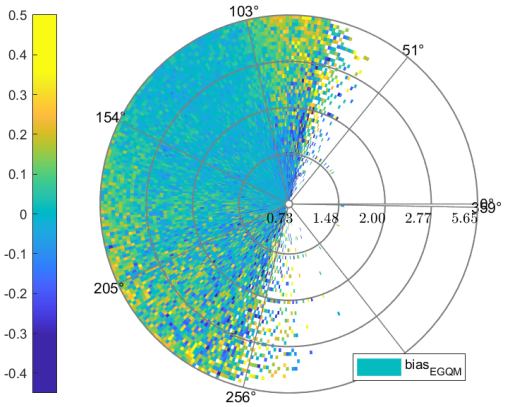

(a) Gumbel quantile mapping bias for Cape Silleiro.

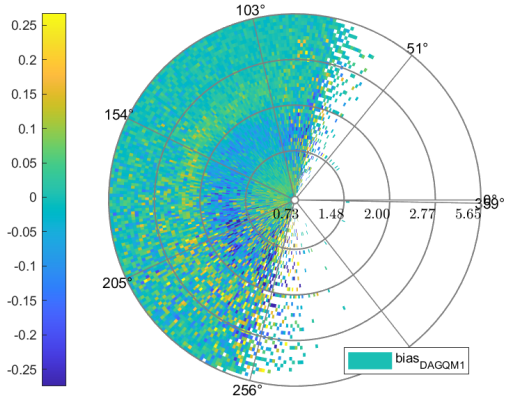

(b) DAGQM bias for Cape Silleiro.

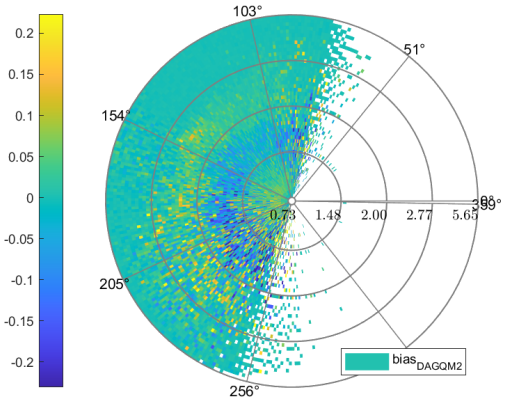

(c) DAGQMrot bias for Cape Silleiro.

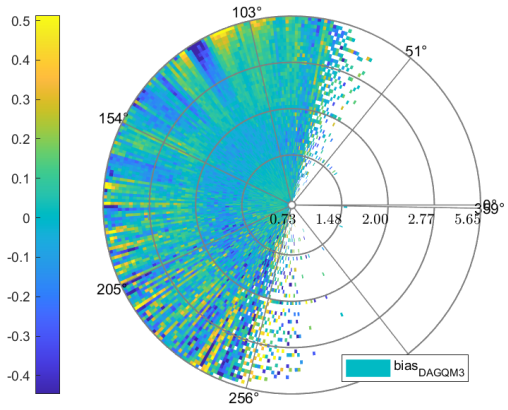

(d) DAGQM2rot bias for Cape Silleiro.

Figure A.11: Mean bias, per quantile and direction, for Gumbel quantile distribution bias correction technique (Cape Silleiro).

cases, with DAGQMrot still outperforming other methods (the attention is called on its colour scale as well, highlighting how it appears the best in terms of bias values and correction's uniformity), and the EGQM plot remarking the different post-correction bias distribution with the techniques that use the wave direction information. Here, not only an uneven correction performance is recorded, but some extremes are not accurately captured and fixed too.
Finally, statistical metrics are available in Figure A.12; as they do not provide any relevant difference with the previous ones (mean bias close to zero for all methods, same dispersion, PDF_{score} and DAV outcomes as the others), the considerations done for the other locations are applied here as well.

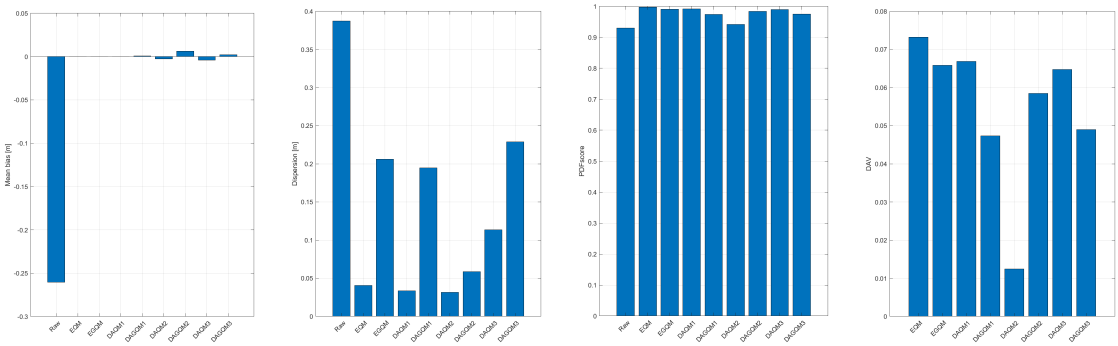

(a) Mean bias. **(b)** Dispersion. **(c)** PDF_{score}. **(d)** DAV.

Figure A.12: Mean bias, dispersion, PDF_{score} and DAV, per each bias correction technique, for Cape Silleiro.

Appendix B

Sensitivity results for all locations

In this second Appendix, the outcomes of the sensitivity analyses are shown, arranged according to the type of sensitivity investigated. Results will be exposed in the same order as the one used in Section 4.2.1.

B.1 Static Identification Window

First on, the Static Identification Window analysis is reported; each location will be displayed time by time.

B.1.1 Cape Creus

In Figure B.1 the output bias and the ratio between the two calibrated datasets (the time-sensitive and the one obtained via contemporaneous correction factors). Just as observed in Gulf of Biscay, the bias still remains within a very good range (rarely exceeding -0.05 or 0.05 m), with only two small peaks in the north-eastern (overestimation) and eastern (underestimation) directions. The ratio shows the same trend observed in Gulf of Biscay too (despite being characterized by slightly higher peaks), with values rarely exceeding 1.6 (typical of some higher quantiles, due to higher wave heights). Differently from what observed in Figure 4.4, though, the plots here do show directional consistency, with bias and ratios observing the same pattern in the same directions in both application periods. As already thought for Gulf of Biscay, this is probably due to the wave distribution in the analysed period: as the id. window is the same, two similarly distributed application periods (as in this case) lead to similar bias directional distribution. The opposite must have happened in the Gulf of Biscay case.

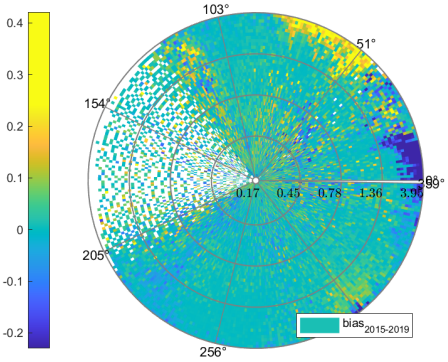

(a) Bias (2015-2019 period).

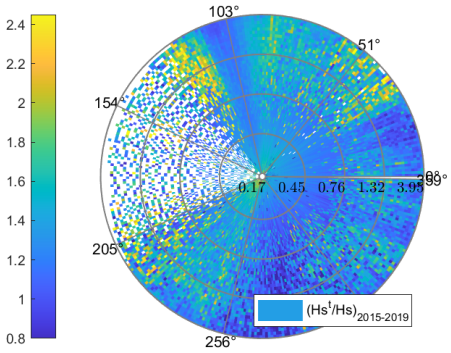

(b) Ratio (2015-2019 period).

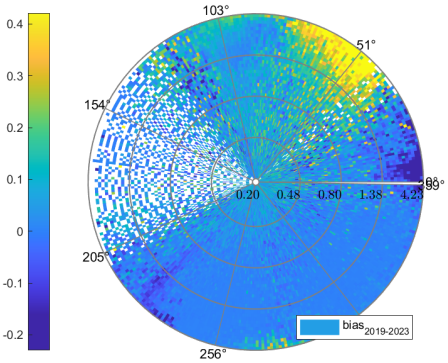

(c) Bias (2019-2023 period).

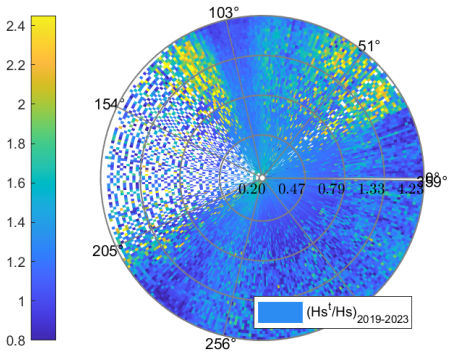

(d) Ratio (2019-2023 period).

Figure B.1: Per each quantile and direction, bias (on the left) and ratio (on the right) heatmaps (2015-2019 above, 2019-2023 below).

For a more statistical perspective, Figure B.2 represents the boxplots and the violinplots for both application periods, reporting forwards and backwards approaches in the two cases.
The results seem to confirm here too what already saw for the Gulf of Biscay analysis. 2015-2019 performs better overall: bias values are closer to the zero line, and boxes' width, whiskers' length and outliers' length are smaller in both approaches (indicating less dispersion, and therefore better consistency in repeatedly correcting the uncertainty on the simulated dataset).
Forwards approach improves its performances from 3 I.Y. on, to reach an optimum around 6 (differently from Gulf of Biscay, results slightly worsen if too many years are used). As in the previous case, backwards analysis' results look less dependent on the number of identification years, appearing constant throughout the whole plots.

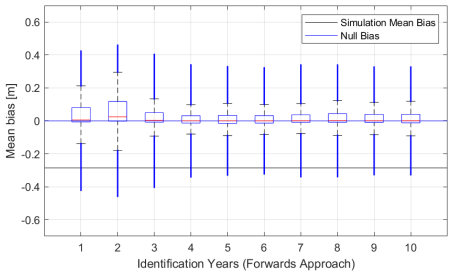

(a) Forward approach, 2015-2019.

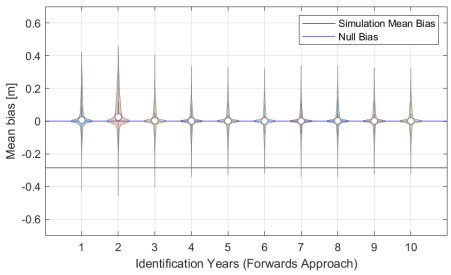

(b) Forward approach, 2015-2019.

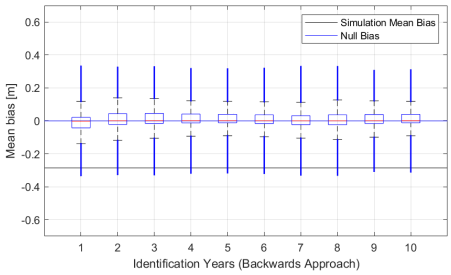

(c) Backwards approach, 2015-2019.

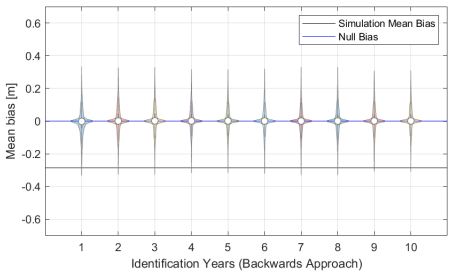

(d) Backwards approach, 2015-2019.

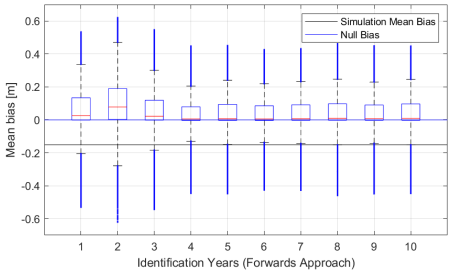

(e) Forwards approach, 2019-2023.

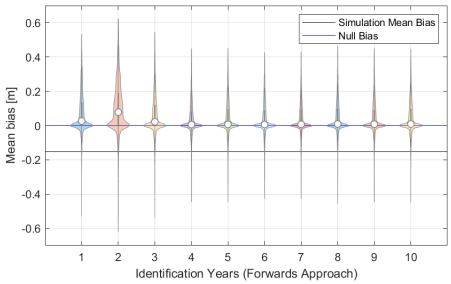

(f) Forwards approach, 2019-2023.

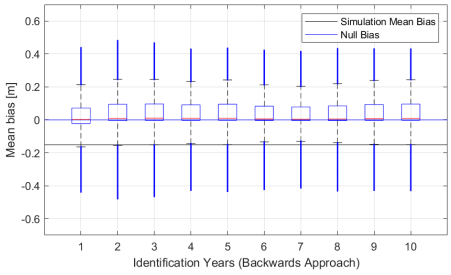

(g) Backwards approach, 2019-2023.

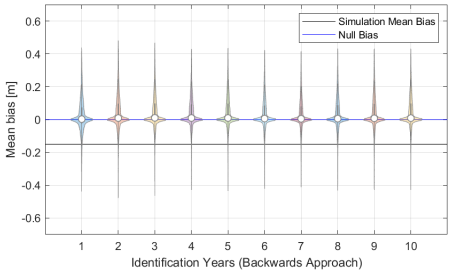

(h) Backwards approach, 2019-2023.

Figure B.2: Boxplots (left) and violinplots (right) for both identification approaches (2015-2019 above, 2019-2023 below).

B.1.2 Gulf of Cadiz

Same order is maintained for Gulf of Cadiz. Figure B.3 shows bias and ratio for the two datasets. Results are coherent with the ones seen until now (with actually even better ratios, indicating better similarity with present-time corrections). Again, bias correction does show a common directional pattern between the two application periods, suggesting that, although different windows are considered, each location's climate is likely to show some consistency throughout the years and, therefore, calibration methods will perform similarly in a given wave direction.

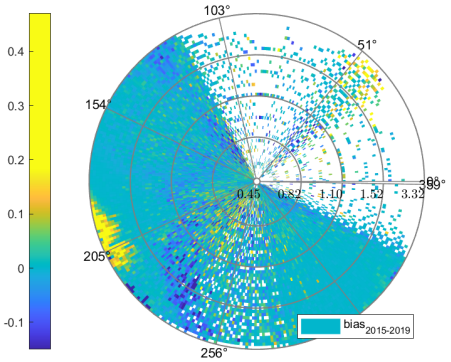

(a) Bias (2015-2019 period).

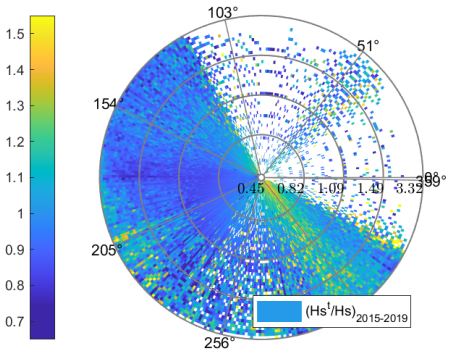

(b) Ratio (2015-2019 period).

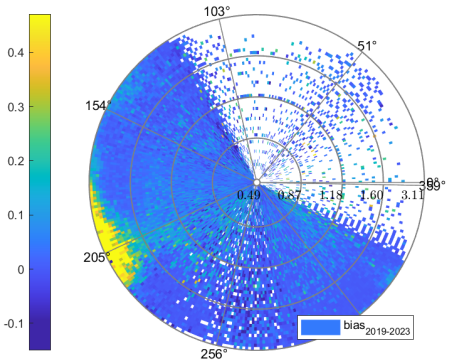

(c) Bias (2019-2023 period).

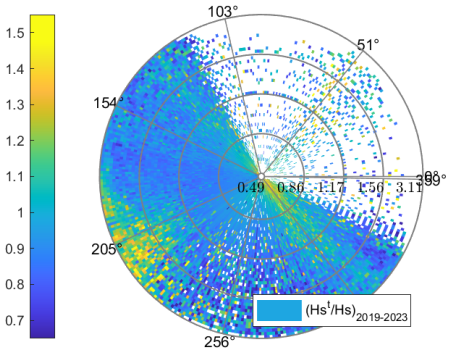

(d) Ratio (2019-2023 period).

Figure B.3: Per each quantile and direction, bias (on the left) and ratio (on the right) heatmaps (2015-2019 above, 2019-2023 below).

In Figure B.3, instead, boxplots and violinplots are reported for the present case study. The strong performance difference between forwards and backwards (much more stable), and (a bit less evident) first and second periods are clear. Both paths seem to be more efficient if at least 4 I.Y. (up to 7, actually, for Figure B.4a) are considered, as first boxes display a too high dispersion.

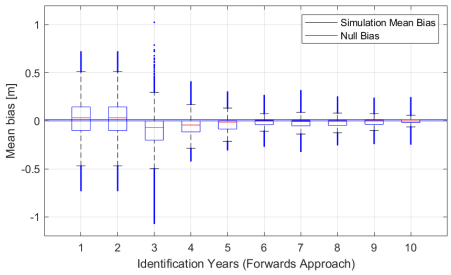

(a) Forward approach, 2015-2019.

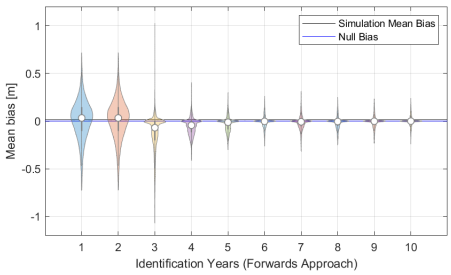

(b) Forward approach, 2015-2019.

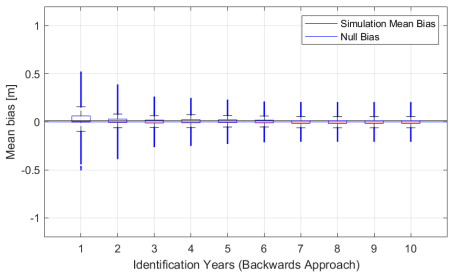

(c) Backwards approach, 2015-2019.

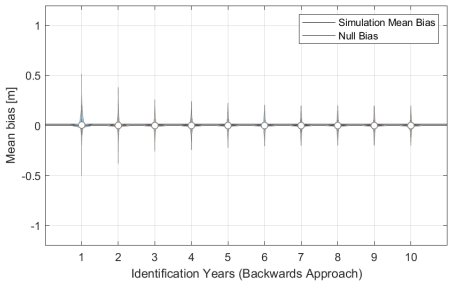

(d) Backwards approach, 2015-2019.

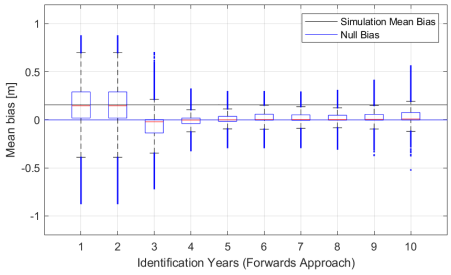

(e) Forwards approach, 2019-2023.

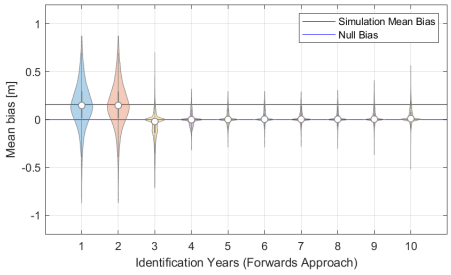

(f) Forwards approach, 2019-2023.

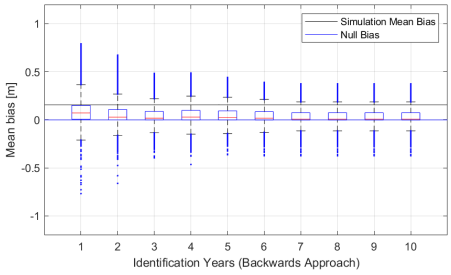

(g) Backwards approach, 2019-2023.

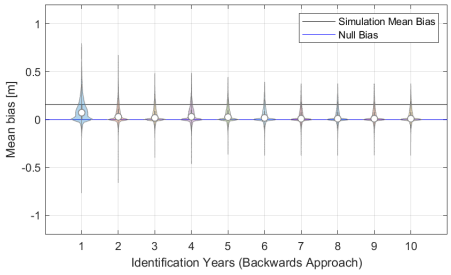

(h) Backwards approach, 2019-2023.

Figure B.4: Boxplots (left) and violinplots (right) for both identification approaches (2015-2019 above, 2019-2023 below).

B.1.3 Cape Silleiro

Finally, the results for Cape Silleiro (the only other location, along with Gulf of Biscay, whose sea-state is dominated by oceanic swell waves) are reported here, starting from bias and ratio plots in Figure B.5. Results keep agreeing to the ones seen until now, both for biases and ratios; for further considerations, the reader is therefore directed to Section 4.2.1.

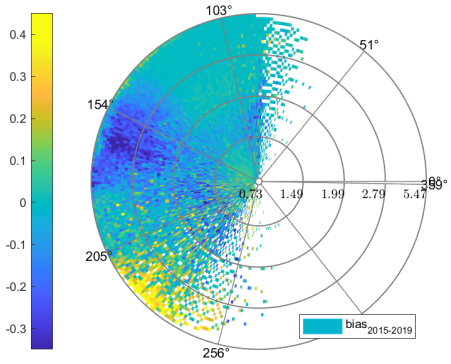

(a) Bias (2015-2019 period).

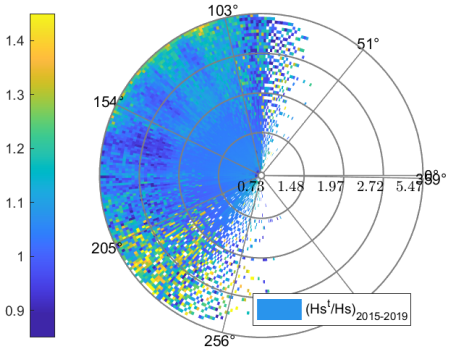

(b) Ratio (2015-2019 period).

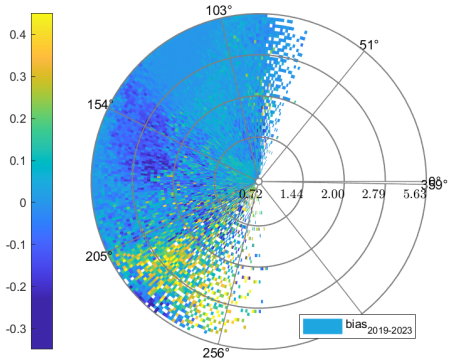

(c) Bias (2019-2023 period).

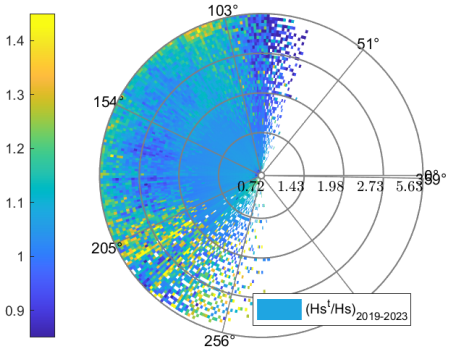

(d) Ratio (2019-2023 period).

Figure B.5: Per each quantile and direction, bias (on the left) and ratio (on the right) heatmaps (2015-2019 above, 2019-2023 below).

In Figure B.6, instead, boxplots and violinplots are represented.
Trends are confirmed here too, with a much more stable pattern observed in the backwards approach; forwards ones stabilize after 6 I.Y., with smaller whiskers, less outliers and much more compact boxes, while the backwards approaches more or less maintain the same satisfactory behavior since 1 I.Y. already.

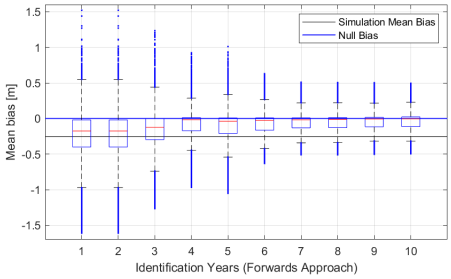

(a) Forward approach, 2015-2019.

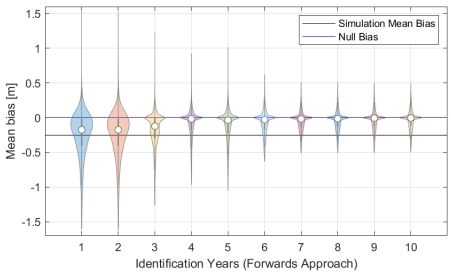

(b) Forward approach, 2015-2019.

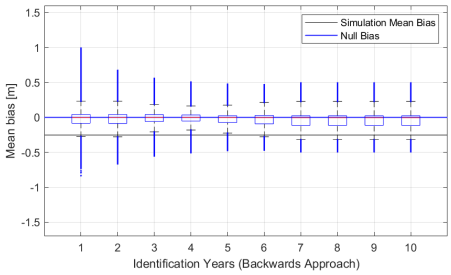

(c) Backwards approach, 2015-2019.

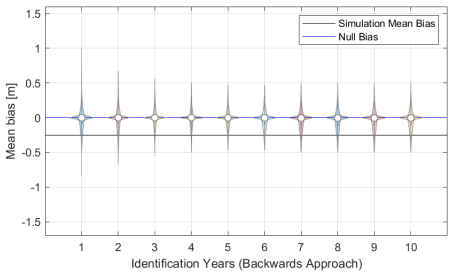

(d) Backwards approach, 2015-2019.

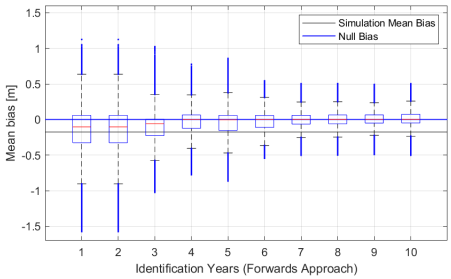

(e) Forwards approach, 2019-2023.

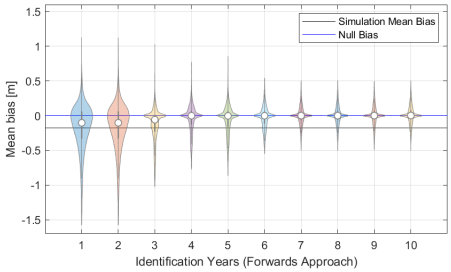

(f) Forwards approach, 2019-2023.

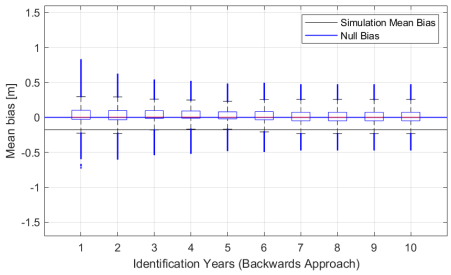

(g) Backwards approach, 2019-2023.

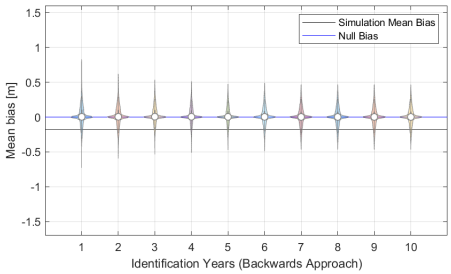

(h) Backwards approach, 2019-2023.

Figure B.6: Boxplots (left) and violinplots (right) for both identification approaches (2015-2019 above, 2019-2023 below).

B.2 Seasonal sensitivity

Finally, results referred to the single-season analysis are represented in this section. The outcomes will be reported separately for each location, with the seasons compared in each case as follows.

B.2.1 Cape Creus

Same location order is maintained here. First on, occurrence scatter diagrams and wave roses (Figure B.7) are displayed, for a proper characterization of each season's climate. In a region that, compared to Gulf of Biscay, shows a higher predominance of wind-seas than swell waves, the distinction between autumn-winter and spring-summer months is even clearer, as the former are characterized by much higher values of H_s (winter showing the highest and more frequent ones, summer the lowest).

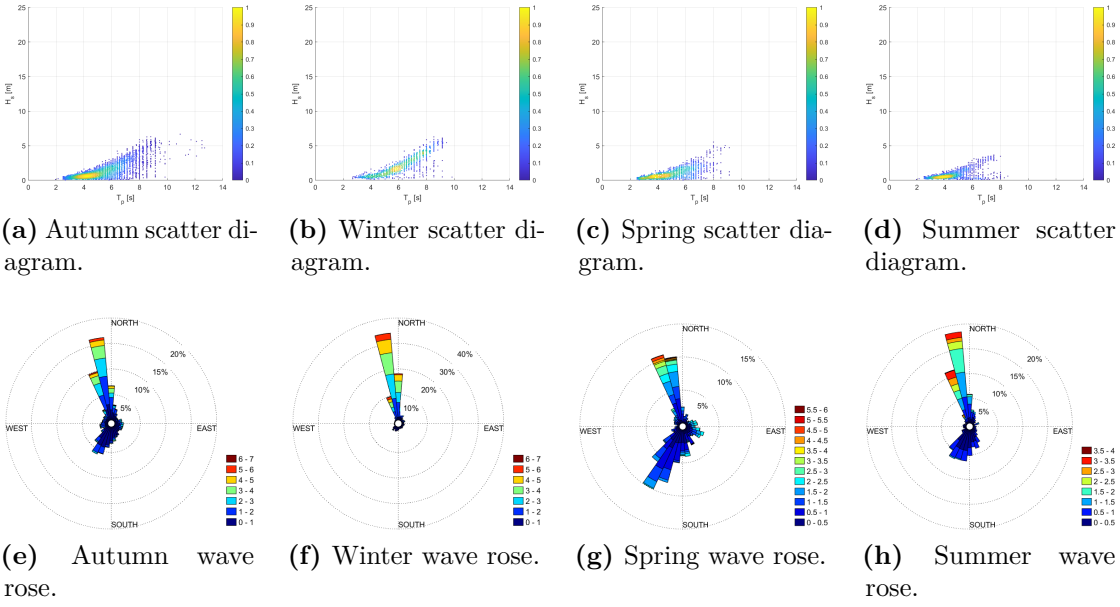

(a) Autumn scatter diagram. **(b)** Winter scatter diagram. **(c)** Spring scatter diagram. **(d)** Summer scatter diagram.

(e) Autumn wave rose. **(f)** Winter wave rose. **(g)** Spring wave rose. **(h)** Summer wave rose.

Figure B.7: Seasonal plots

Hence, Figure B.8 reports the results of the calibration process carried out with correction factors obtained from each different season. The scales have been, again, purposely kept different, to let the reader seize how different the bias entity can be between each case.
First, it can be noted that, being the region characterized by overall lower wave heights than the oceanic swell ones typical of Gulf of Biscay, the underestimation

risk is generally lower. In fact, autumn (which, again, shows the lowest bias peaks) and winter (the one with lowest bias in most areas) plots tend to overestimate some extremes in waves coming from north (west too, speaking about Figure B.8a). Performances drop a bit as spring factors are used, with a higher spread of underestimated (or overestimated, in some upper eastern quantiles) wave heights and an increased average bias; summer, finally, shows again an even more serious underestimation issue of the extremes in some of the most common wave directions (south-west, in this case), as a consequence of the poor information availability in the upper quantiles of those regions of the wave roses.

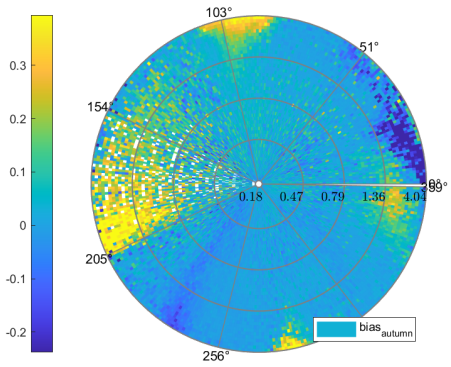

(a) Autumn.

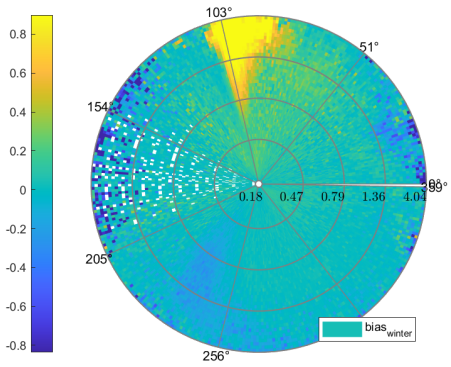

(b) Winter.

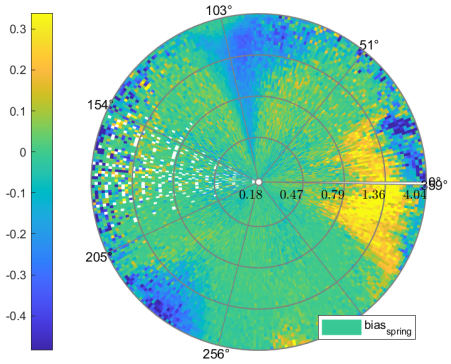

(c) Spring.

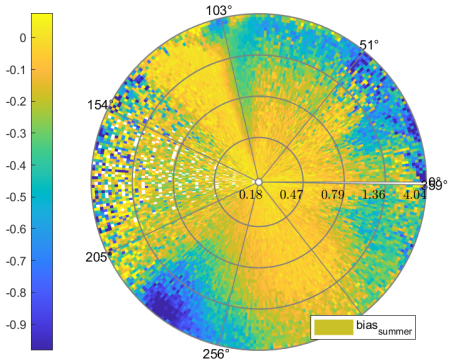

(d) Summer.

Figure B.8: Average bias per each quantile and direction in every season of the year (Cape Creus, 2012).

Figure B.9, finally, shows the same boxplots as in Figure 4.14, comparing each season against each other and with the 1-year and present-time reference. Compared to the Gulf of Biscay ones displayed in Figure 4.14, the lower bias values are immediately clear (as some whiskers' peaks were previously close to 3 m, while here they don't overcome the 1 m threshold).

Boxplots immediately highlight again summer as the worst season, while the quality of present-time bias correction is confirmed. Spring and winter show quite similar box's width and centering (with spring's median bias actually better coinciding with the zero-line), although autumn confirms as the best season. In fact, Cape Creus confirms that the autumn's correction factor provide even slightly better results than the whole-year case, in terms both of box's width and outliers' number, highlighting how it may not be worth gathering a whole year of data, and that the autumn dataset itself looks perfectly reliable for a proper data calibration.

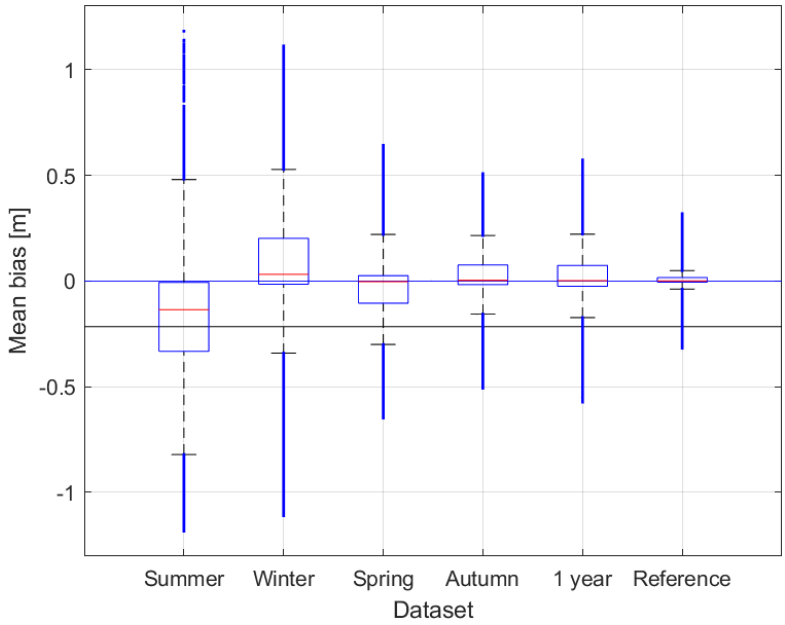

Figure B.9: Boxplots comparing each season of the year 2012 (Cape Creus).

B.2.2 Gulf of Cadiz

Moving to the Gulf of Cadiz, each season's climate is characterized in the occurrence scatter diagrams and wave roses reported in Figure B.10, respectively.
It sticks out that, despite being partially more open to oceanic swells than Cape Creus, it is the one showing, by far, the lowest wave heights among the seasonal plots showed until now.
In this case too, both type of plots display autumn showing the biggest probability of experiencing high waves and better covering the whole spectre of possible sea-states. Spring and (even more) summer, on the other hand, are characterized by much lower H_s values, suggesting again some likely difficulties in providing correction factors for the highest quantiles.

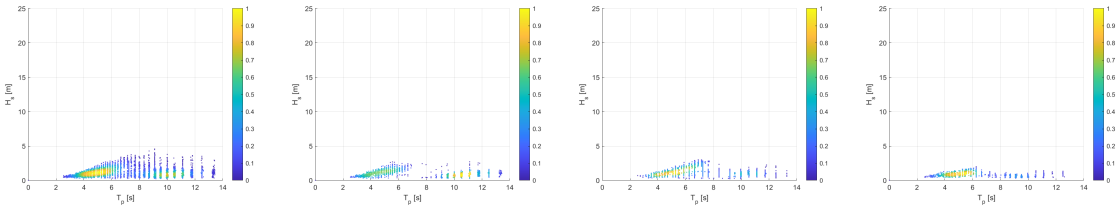

(a) Autumn scatter diagram.

(b) Winter scatter diagram.

(c) Spring scatter diagram.

(d) Summer scatter diagram.

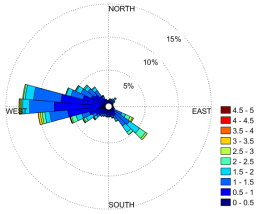

(e) Autumn wave rose.

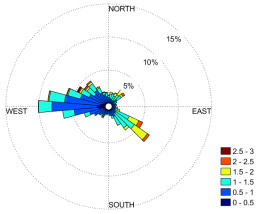

(f) Winter wave rose.

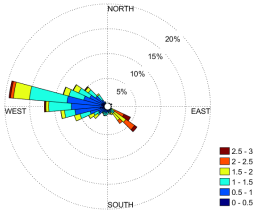

(g) Spring wave rose.

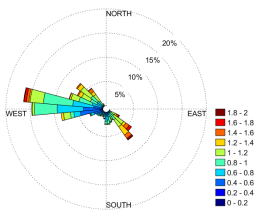

(h) Summer wave rose.

Figure B.10: Seasonal plots

In Figure B.11 shows again the results of the bias corrections carried out via single-season correction factors.
Coherently to what already stated for Cape Creus, the even lower average wave height reflects in lower bias values as well.
Here, curiously, winter is the season producing the highest underestimation in upper quantiles from south-western direction (followed by summer, as already happened in all other locations). Autumn, on the other hand, is again the best season by far, with a bias close to zero in most regions of the heatmap, and a slighter underestimation in the same extreme regions of the south-western directions.

The boxplot in Figure B.12 allows again a visual comparison of the results from a statistic point of view.
Being the efficiency of the reference present-time correction proven here too, the seasons' comparison shows winter being the worst season this time, differently from what seen until now, as a result of its strong underestimation in some regions of the plot. Summer confirms itself as a non-optimal fit for the region; spring provides slightly better performances, although autumn is, once again, the best option for correction factors' identification.
In fact, it still provides better results than the whole-year reference, in terms of bias dispersion especially.

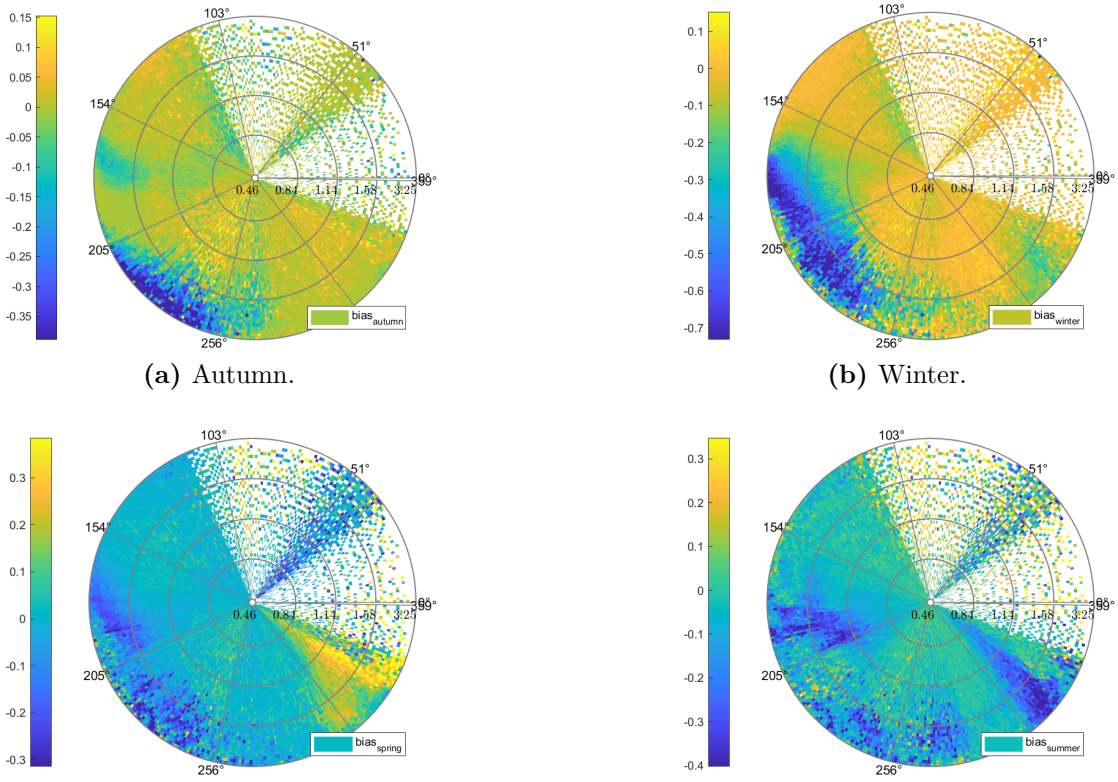

(a) Autumn.

(b) Winter.

(c) Spring.

(d) Summer.

Figure B.11: Average bias per each quantile and direction in every season of the year (Gulf of Cadiz, 2012).

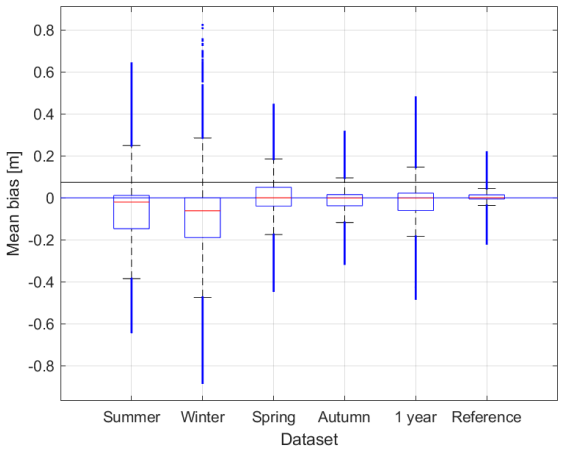

Figure B.12: Boxplots comparing each season of the year 2012 (Gulf of Cadiz).

B.2.3 Cape Silleiro

Cape Silleiro is the last location considered; it is, as Gulf of Biscay, open to the Atlantic ocean, and therefore dominated by swell waves. Their effect are clear, looking at both occurrence diagrams and wave roses (Figure B.13), as they cause much higher values of H_s; the same seasonal trend as the other locations is respected here.

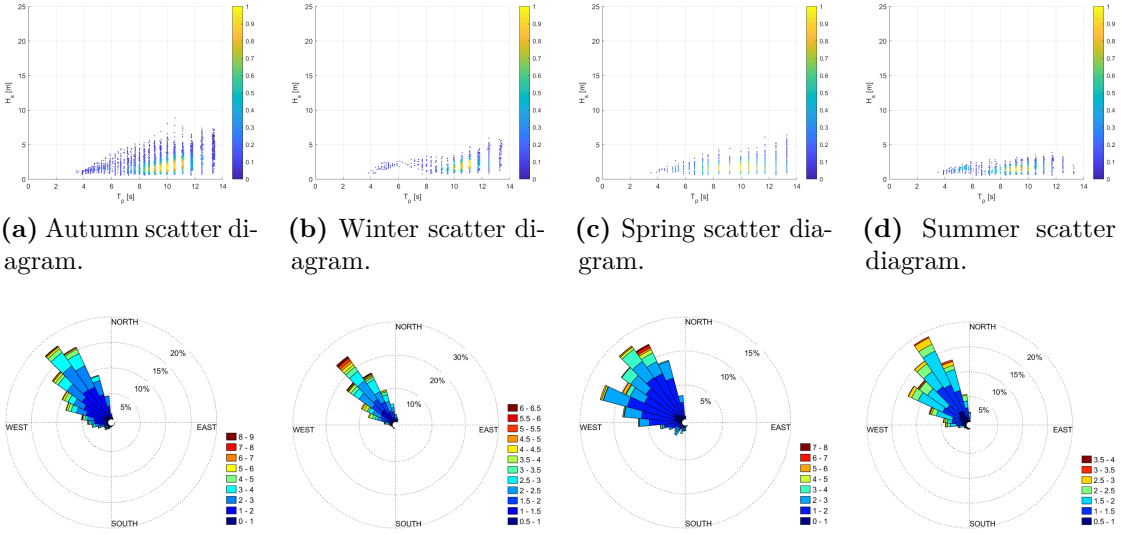

(a) Autumn scatter diagram. **(b)** Winter scatter diagram. **(c)** Spring scatter diagram. **(d)** Summer scatter diagram.

(e) Autumn wave rose. **(f)** Winter wave rose. **(g)** Spring wave rose. **(h)** Summer wave rose.

Figure B.13: Seasonal plots

Just as for Gulf of Biscay, higher swell waves result in higher bias values. Still, comparing all seasons, overall patterns are validated once again.
Heatmaps keep being displayed with different colour scales. Summer keeps showing its underestimation issues (on western waves especially), due to the lack of high waves for calibration, while autumn keeps being the best: both bias representation and, most of all, boxplots clearly show its very good median bias combined with a very low dispersion and number of outliers. Most importantly, all locations agree on showing autumn as even better than a whole-year analysis, confirming that is does represent a viable option for identifying correction factors to be applied on a future time window.

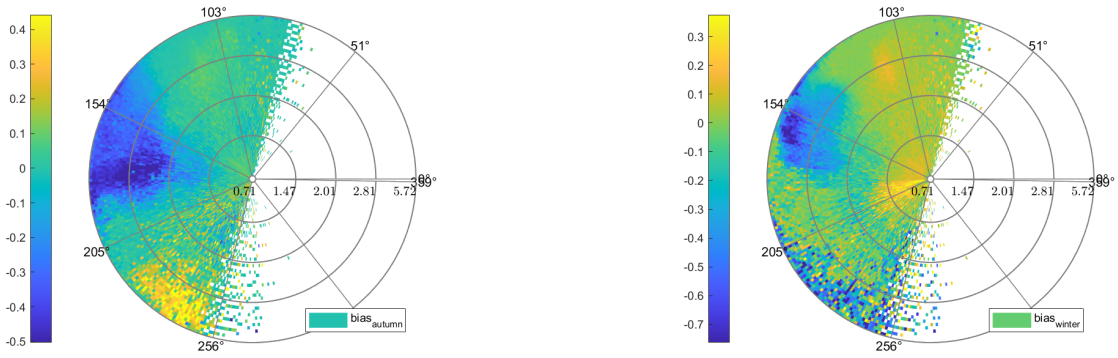

(a) Autumn. **(b)** Winter.

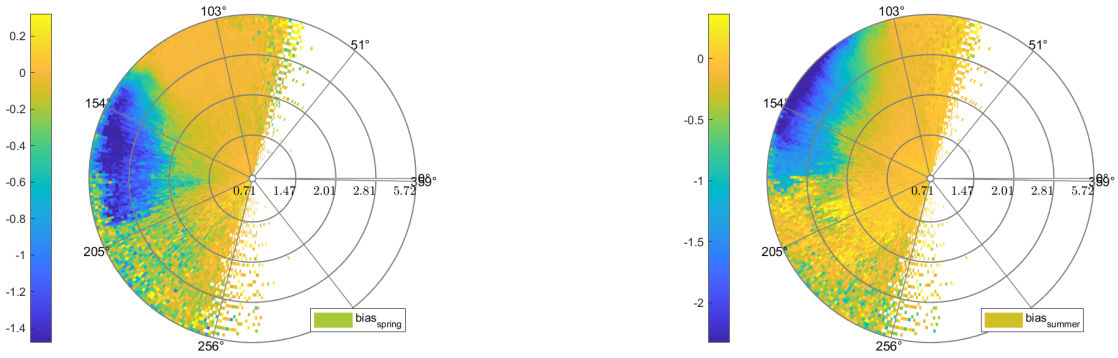

(c) Spring. **(d)** Summer.

Figure B.14: Average bias per each quantile and direction in every season of the year (Cape Silleiro, 2012).

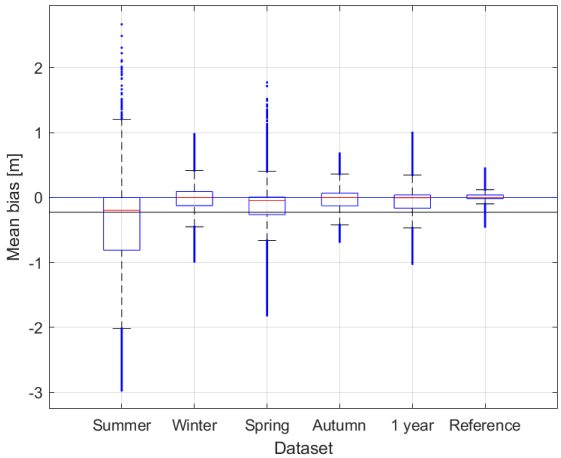

Figure B.15: Boxplots comparing each season of the year 2012 (Cape Silleiro).

Bibliography

[1] International Renewable Energy Agency (IRENA). *Future of Wind: Deployment, investment, grid integration and socio-economic aspects (A Global Energy Transformation paper)*. Tech. Rep. Abu Dhabi: International Renewable Energy Agency, Apr. 2019. URL: https://www.irena.org/publications/2019/Apr/Global-energy-transformation-A-roadmap-to-2050-2019Edition (cit. on p. 1).

[2] International Energy Agency (IEA). *Net Zero by 2050: A Roadmap for the Global Energy Sector*. Tech. rep. International Energy Agency (IEA), 2021. URL: https://iea.blob.core.windows.net/assets/deebef5d-0c34-4539-9d0c-10b13d840027/NetZeroby2050-ARoadmapfortheGlobalEnergySector_CORR.pdf (cit. on p. 1).

[3] National Renewable Energy Laboratory (NREL). *Wind Energy Technologies Office 2020 Peer Review: Offshore Wind Energy Conversion System Reliability and O&M Tools*. Tech. rep. NREL/TP-5000-78773. National Renewable Energy Laboratory (NREL), 2021. URL: https://www.nrel.gov/docs/fy21osti/78773.pdf (cit. on p. 1).

[4] Martinez A. Penalba M. Aizpurua J. «On the definition of a risk index based on long term metocean data to assist in the design of Marine Renewable Energy systems». In: *Ocean Engineering* 242 (Dec. 2021), p. 110080. DOI: 10.1016/j.oceaneng-2021.110080 (cit. on p. 2).

[5] International Organization for Standardization (ISO). *ISO 19901-1:2015 Petroleum and natural gas industries — Specific requirements for offshore structures — Part 1: General requirements*. Tech. rep. ISO, 2015. URL: https://www.iso.org/obp/ui/en/#iso:std:iso:19901:-1:ed-2:v1:en (cit. on pp. 2, 23).

[6] Science The Institute of Marine Engineering and Technology (IMarEST). *IMarEST Metocean Procedures Guide*. Tech. rep. The Institute of Marine Engineering, Science and Technology (IMarEST), 2018. DOI: 10.13140/RG.2.2.18997.52960 (cit. on pp. 2, 23).

[7] A. Ulazia, M. Penalba, G. Ibarra-Berastegui, J. Ringwood, and J. Saenz. «Wave energy trends over the Bay of Biscay and the consequences for wave energy converters». In: *Energy* 141 (2017), pp. 624–634. DOI: https://doi.org/10.1016/j.energy.2017.09.099. URL: https://www.sciencedirect.com/science/article/pii/S0360544217316183 (cit. on p. 3).

[8] J. Saenz S. Carreno-Madinabeitia G. Ibarra-Berastegui and A. Ulazia. «Long-term changes in offshore wind power density and wind turbine capacity factor in the Iberian Peninsula (1900–2010)». In: *Energy* 226 (2021), p. 120364. DOI: https://doi.org/10.1016/j.energy.2021.120364. URL: https://www.sciencedirect.com/science/article/pii/S0360544221006137 (cit. on p. 3).

[9] G. Lemos, M. Menendez, A. Semedo, P. Camus, M. Hemer, M. Dobrynin, and P. M. A. Miranda. «On the need of the bias correction methods for wave climate projections». In: *Global and Planetary Change* (2020), p. 103109. DOI: https://doi.org/10.1016/j.gloplacha.2019.103109. URL: https://www.sciencedirect.com/science/article/pii/S0921818119305946 (cit. on pp. 3–7, 9).

[10] M. Penalba, G. Chao, A. Zarketa-Astigarraga, G. Cervelli, G. Giorgi, and B. Robertson. «Bias correction techniques for uncertainty reduction of long-term metocean data for ocean renewable energy systems». In: *Renewable Energy* 219 (Oct. 2023), p. 119404. DOI: 10.1016/jrenene.2023.119404 (cit. on pp. 3–6, 12, 16).

[11] M. Menendez J. Perez and I. J. Losada. In: *Coastal Engineering* (2017). ISSN: 0378-3839. DOI: https://doi.org/10.1016/j.coastaleng.2017.03.005. URL: https://www.sciencedirect.com/science/article/pii/S0378383917300443 (cit. on p. 4).

[12] Douglas Maraun. «Bias Correcting Climate Change Simulations - a Critical Review». In: *Current Climate Change Reports* 2 (2016), pp. 211–220. DOI: 10.1007/s40641-016-0050-x. URL: https://doi.org/10.1007/s40641-016-0050-x (cit. on p. 4).

[13] U. Ehret, E. Zehe, V. Wulfmeyer, K. Warrach-Sagi, and J. Liebert. «HESS Opinions "Should we apply bias correction to global and regional climate model data?"» In: *Hydrology and Earth System Sciences* 16.9 (2012), pp. 3391–3404. DOI: 10.5194/hess-16-3391-2012. URL: https://hess.copernicus.org/articles/16/3391/2012/ (cit. on p. 4).

[14] G. H. Leavesley L. E. Hay R. L. Wilby. «A comparison of delta change and downscaled GCM scenarios for three mountainous basins in the United States». In: *Journal of the American Water Resources Association* 36 (2000), pp. 387–397. DOI: 10.1111/j.1752-1688.2000.tb04276.x (cit. on p. 4).

[15] E. J. Gumbel. «Les valeurs extrêmes des distributions statistiques». In: *Annales de l'institut Henri Poincaré* (1935) (cit. on p. 5).

[16] R. Minguez, A. Espejo, A. Tomàs, F.J. Mendez, and I.J. Losada. «Directional Calibration of Wave Reanalysis Databases Using Instrumental Data». In: *Journal of Atmospheric and Oceanic Technology* 18.11 (2011), pp. 1466–1485. DOI: 10.1175/JTECH-D-11-00008.1. URL: https://journals.ametsoc.org/view/journals/atot/28/11/jtech-d-11-00008_1.xml (cit. on p. 7).

[17] A. Semedo, K. Suselj, A. Rutgersson, and A. Sterl. «A Global View on the Wind Sea and Swell Climate and Variability from ERA-40». In: *Journal of Climate* 24.5 (2011), pp. 1461–1479. DOI: 10.1175/2010JCLI3718.1. URL: https://journals.ametsoc.org/view/journals/clim/24/5/2010jcli3718.1.xml (cit. on p. 7).

[18] A. Semedo et al. «CMIP5-Derived Single-Forcing, Single-Model, and Single-Scenario Wind-Wave Climate Ensemble: Configuration and Performance Evaluation». In: *Journal of Marine Science and Engineering* 6 (2018). DOI: 10.3390/jmse6030090. URL: https://www.mdpi.com/2077-1312/6/3/90 (cit. on p. 7).

[19] F. Collard F. Ardhuin B. Chapron. «Observation of swell dissipation across oceans». In: *Geophysical Research Letters* 36 (2009). DOI: 10.1029/2008GL037030 (cit. on p. 7).

[20] BIMEP. *Mutriku Wave Power Plant*. Accessed: 21/5/2024. URL: https://www.bimep.com/en/mutriku-area/%20technical-characteristics/ (cit. on p. 12).

[21] Saitec O. T. *Geroa - precommercial project*. Accessed: 21/5/2024. URL: https://saitec-offshore.com/en/projects/geroa/ (cit. on p. 12).

[22] Sarah Perkins-Kirkpatrick, A. Pitman, Neil Holbrook, and John Mcaneney. «Evaluation of the AR4 Climate Models' Simulated Daily Maximum Temperature, Minimum Temperature, and Precipitation over Australia Using Probability Density Functions». In: *Journal of Climate* 20 (Sept. 2007). DOI: 10.1175/JCLI4253.1 (cit. on p. 16).